INTERNATIONAL JOURNAL FOR NUMERICAL METHODS IN FLUIDS
Int. J. Numer. Meth. Fluids 2006; **50**:309–345
Published online 1 September 2005 in Wiley InterScience (www.interscience.wiley.com). DOI: 10.1002/fld.1059

Flux and source term discretization in two-dimensional shallow water models with porosity on unstructured grids

Vincent Guinot[1,*,†] and Sandra Soares-Frazão[2,‡]

[1]*HydroSciences Montpellier, UMR 5569 (UM1, UM2, IRD, CNRS), Université Montpellier 2, Maison des Sciences de l'Eau, 34095 Montpellier Cedex 5, France*
[2]*FNRS—Université catholique de Louvain-la-Neuve, Unité de Génie Civil et Environnemental, Place du Levant, 1, B-1348 Louvain-la-Neuve, Belgium*

SUMMARY

Two-dimensional shallow water models with porosity appear as an interesting path for the large-scale modelling of floodplains with urbanized areas. The porosity accounts for the reduction in storage and in the exchange sections due to the presence of buildings and other structures in the floodplain. The introduction of a porosity into the two-dimensional shallow water equations leads to modified expressions for the fluxes and source terms. An extra source term appears in the momentum equation. This paper presents a discretization of the modified fluxes using a modified HLL Riemann solver on unstructured grids. The source term arising from the gradients in the topography and in the porosity is treated in an upwind fashion so as to enhance the stability of the solution. The Riemann solver is tested against new analytical solutions with variable porosity. A new formulation is proposed for the macroscopic head loss in urban areas. An application example is presented, where the large scale model with porosity is compared to a refined flow model containing obstacles that represent a schematic urban area. The quality of the results illustrates the potential usefulness of porosity-based shallow water models for large scale floodplain simulations. Copyright © 2005 John Wiley & Sons, Ltd.

KEY WORDS: shallow water equations; Riemann solver; Godunov-type schemes; porosity; analytical solutions; hyperbolic systems of conservation laws

1. INTRODUCTION

The recent interest for flood simulation involving urbanized areas [1–6] has drawn the attention to the possible use of modified shallow water models with porosity for large scale flood

*Correspondence to: Vincent Guinot, HydroSciences Montpellier, UMR 5569 (UM1, UM2, IRD, CNRS), Université Montpellier 2, Maison des Sciences de l'Eau, 34095 Montpellier Cedex 5, France.
†E-mail: guinot@msem.univ-montp2.fr
‡E-mail: soares@gce.ucl.ac.be

Contract/grant sponsor: Université catholique de Louvain-la-Neuve

Received 29 October 2004
Revised 26 June 2005
Accepted 3 July 2005

simulations involving urbanized areas. The modified shallow water equations with porosity were first introduced in a simplified form by Defina *et al.* [7] and later modified by Hervouet *et al.* [8]. In these modified equations the porosity accounts for the presence of buildings, structures, etc. that restrict the area available to water flow. The influence of the porosity is twofold in that it expresses a restriction in (i) the area locally available to mass and momentum storage and (ii) the mass and momentum fluxes in both directions of space. Shallow water models with porosity have a direct interest to floodplain and urban flood modelling in that they allow the influence of urbanized areas on the flow to be represented using the statistical properties of the urban network, without the need for a detailed description of the urban geometry and the subsequent mesh refinement. Shallow water models with porosity may therefore be used for large-scale simulations of flood-induced transients. The simulation results may then be extracted and interpolated to provide boundary conditions to local, refined flow models where the details of the urban areas are represented. Another possible use of such models is the simulation of floodplain behaviour in the presence of urbanized areas that condition partly the behaviour of the floodplain, but where the details of the flow within the urban areas are not of direct interest.

The addition of a spatially varying porosity to the classical two-dimensional shallow water equations yields additional source terms in the modified equations. Although similar in structure to the source terms induced by the topographical gradient, the porosity-induced source term triggers the need for a specific treatment of both the continuity and momentum equations. The treatment of topographical source terms within Godunov-type algorithms [9] for the solution of the classical shallow water equations has been the subject of intensive research (see e.g. References [10–16] and the references therein for the derivation and application of the various approaches available). The present paper aims (i) to propose an approximate Riemann solver for the modified shallow water equations with porosity written in conservation form on unstructured grids, coupled with an upwind treatment of source terms, (ii) to provide new analytical and semi-analytical test cases that can be used as a basis for numerical method assessment, and (iii) to provide a path for the determination of the macroscopic friction source term that accounts for energy loss due to wave reflections against obstacles in the porous zone. Solving the equations in conservation form allows discontinuous solutions (such as hydraulic jumps, bores, etc.) to be computed accurately. The proposed solver is based on the Harten-Lax-van Leer (HLL) formalism. The fluxes and source terms are computed within the same step and the source terms are treated in an upwind fashion so as to satisfy equilibrium and steady-state conditions. Section 2 presents the governing equations. Section 3 details the computation of the fluxes and source terms. Section 4 is devoted to computational examples. Section 5 provides concluding remarks.

2. GOVERNING EQUATIONS

The shallow water equations with porosity (see Appendix A for a detailed derivation) can be written in conservation form as

$$\frac{\partial}{\partial t}(\phi \mathbf{U}) + \frac{\partial}{\partial x}(\phi \mathbf{F}) + \frac{\partial}{\partial y}(\phi \mathbf{G}) = \mathbf{S} \tag{1}$$

with

$$\mathbf{U}=\begin{bmatrix} h \\ hu_x \\ hu_y \end{bmatrix}, \quad \mathbf{F}=\begin{bmatrix} hu_x \\ hu_x^2+gh^2/2 \\ hu_xu_y \end{bmatrix}, \quad \mathbf{G}=\begin{bmatrix} hu_y \\ hu_xu_y \\ hu_y^2+gh^2/2 \end{bmatrix}, \quad \mathbf{S}=\begin{bmatrix} 0 \\ S_{0,x}+S_{f,x} \\ S_{0,y}+S_{f,y} \end{bmatrix} \tag{2}$$

where g is the gravitational acceleration, h is the water depth, u_x and u_y are the x- and y-velocities, respectively, $S_{0,x}$ and $S_{0,y}$ are the source terms arising from the bottom slopes and porosity variations in the x- and y-directions, respectively, $S_{f,x}$ and $S_{f,y}$ are the source terms arising from friction in the x- and y-directions, respectively, and ϕ is the porosity. In what follows, ϕ is assumed to depend on the space coordinates only. The topographical source terms are given by

$$\begin{aligned} S_{0,x} &= -\phi gh\frac{\partial z_b}{\partial x}+g\frac{h^2}{2}\frac{\partial \phi}{\partial x} \\ S_{0,y} &= -\phi gh\frac{\partial z_b}{\partial y}+g\frac{h^2}{2}\frac{\partial \phi}{\partial y} \end{aligned} \tag{3}$$

where z_b is the bottom elevation. The first term on the right-hand side of Equation (3) accounts for variations in the bottom level. The resulting force on the water body is exerted only on a fraction ϕ of the total section of the control volume. The second term on the right-hand side accounts for the longitudinal variations in the porosity. The friction terms are assumed to result from (i) the bottom and wall shear stress, accounted for by Strickler's law, and (ii) the energy losses triggered by the flow regime variations and the multiple wave reflections against obstacles in the porous zone, accounted for by a classical head loss formulation

$$\begin{aligned} S_{f,x} &= -\phi gh\frac{(u_x^2+u_y^2)^{1/2}}{K^2h^{4/3}}u_x-\phi ghs_x(u_x^2+u_y^2)^{1/2}u_x \\ S_{f,y} &= -\phi gh\frac{(u_x^2+u_y^2)^{1/2}}{K^2h^{4/3}}u_y-\phi ghs_y(u_x^2+u_y^2)^{1/2}u_y \end{aligned} \tag{4}$$

where K is the Strickler coefficient (assumed to be isotropic in the present paper) and s_x and s_y are head loss coefficients accounting for the singular head losses due to the urban singularities in the x- and y-directions, respectively. The choice of this formulation is justified in Appendix B. Equation (1) can be rewritten in non-conservation (or characteristic) form as

$$\frac{\partial}{\partial t}(\phi\mathbf{U})+\mathbf{A}\frac{\partial}{\partial x}(\phi\mathbf{U})+\mathbf{B}\frac{\partial}{\partial y}(\phi\mathbf{U})=\mathbf{S} \tag{5}$$

It is easy to check that the matrices $\mathbf{A}$ and $\mathbf{B}$ are identical to the characteristic matrices of the classical shallow water equations (i.e. the equations obtained by taking $\phi=1$). Therefore, the structure and properties of the solution (number of waves and characteristic surfaces, wave celerities and Riemann invariants) are identical to those of the solutions of the classical shallow water equations. In what follows, Equation (1) is discretized using the finite volume

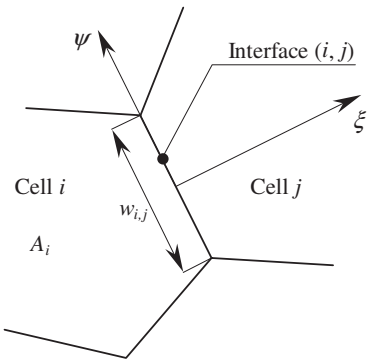

Figure 1. Definition sketch of the finite volume discretization.

approach on unstructured grids (Figure 1)

$$\mathbf{U}_i^{n+1} = \mathbf{U}_i^n - \frac{\Delta t}{\phi_i A_i} \sum_{j \in N(i)} \mathbf{P}_{i,j} (\phi \mathbf{F})_{i,j}^{n+1/2} w_{i,j} + \frac{\Delta t}{\phi_i} \mathbf{S}_i^{n+1/2} \tag{6}$$

$\mathbf{U}_i^n$ is the average value of $\mathbf{U}$ over the cell i at the time level n, A_i is the area of the cell i, $\mathbf{F}_{i,j}^{n+1/2}$ is the average value of the flux vector in the direction normal to the interface (i, j) between the time levels n and $n+1$, $N(i)$ is the set of neighbour cells of the cell i, $\mathbf{P}_{i,j}$ is the matrix that accounts for the coordinate change from the global (x, y) coordinate system attached to the interface, $w_{i,j}$ is the width of the interface (i, j), $\mathbf{S}_i^{n+1/2}$ is the average value over the cell i between the time levels n and $n+1$ of the source term arising from the bottom slope, porosity gradient and friction and Δt is the computational time step. The components of $\mathbf{S}_i^{n+1/2}$ are given by Equations (3) and (4). The matrix $\mathbf{P}_{i,j}$ expresses the rotation from the global coordinate system (x, y) to the local coordinate system (ξ, ψ) attached to the interface. The rotation leaves the water depth invariant and acts on the x- and y-unit discharges. The expression of $\mathbf{P}_{i,j}$ is therefore

$$\mathbf{P}_{i,j} = \begin{bmatrix} 1 & 0 & 0 \\ 0 & n_{i,j}^{(x)} & -n_{i,j}^{(y)} \\ 0 & n_{i,j}^{(y)} & n_{i,j}^{(x)} \end{bmatrix} \tag{7}$$

where $n_{i,j}^{(x)}$ and $n_{i,j}^{(y)}$ are the x- and y-components, respectively, of the normal unit vector between the cells i and j (oriented positive from i to j).

The flux $\mathbf{F}$ at the interface is computed using the following procedure. In a first step, the Riemann problem in the global coordinate system (x, y) is transformed to the local coordinate system (ξ, ψ) via a left-hand multiplication by $\mathbf{P}_{i,j}^{-1}$. In a second step, the local Riemann problem is solved using a modified Harten-Lax-van Leer (HLL) Riemann solver [17, 18] described in Section 3. Eventually, the flux is transformed back to the (x, y) coordinate system, as in Equation (6).

3. FLUX AND SOURCE TERM COMPUTATION

In what follows it is assumed that the flow variables are available at the computational time t^n. The flow variables may have been reconstructed using any higher-order technique (e.g. a multidimensional or dimensionally split MUSCL reconstruction [19]). The reconstruction allows Riemann problems to be defined at each interface (i, j) between two adjacent cells i and j. The Riemann problem is an initial value problem where the initial value of $\mathbf{U}$ is piecewise constant, equal to $\mathbf{U}_\mathrm{L}$ and $\mathbf{U}_\mathrm{R}$ on the left- and right-hand side of the interface, respectively (see References [20, 21] for an overview of the various options available to define $\mathbf{U}_\mathrm{L}$ and $\mathbf{U}_\mathrm{R}$ from the reconstructed variables). In what follows the source term arising from the bottom slope and the variations in the porosity is computed within the same step as the fluxes. This step is described in Sections 3.1–3.3. The source term arising from friction is accounted for in a separate step, described in Section 3.4.

3.1. Overview of the algorithm

The present subsection focuses on the discretization of the flux $\mathbf{F}$ and the part of the source term that arises from the bottom slope and the porosity gradient. As mentioned above the friction source term is accounted for in a separate step. It is assumed in what follows that a one-dimensional Riemann problem has been defined in the local coordinate system attached to the interface as explained in the previous section. The equation to be solved in the direction normal to the interface reduces to

$$\frac{\partial}{\partial t}(\phi\mathbf{U}) + \frac{\partial}{\partial \xi}(\phi\mathbf{F}) = \mathbf{S}_0 \tag{8}$$

with

$$\mathbf{U} = \begin{bmatrix} h \\ hu \\ hv \end{bmatrix}, \quad \mathbf{F} = \begin{bmatrix} hu \\ hu^2 + gh^2/2 \\ huv \end{bmatrix}, \quad \mathbf{S}_0 = \begin{bmatrix} 0 \\ S_{0,\xi} \\ 0 \end{bmatrix} \tag{9}$$

where u and v are the velocity components in the direction normal and tangent to the interface, respectively, and should not be confused with the velocity components u_x and u_y in the original (x, y) coordinate system. The source term $S_{0,\xi}$ in the direction normal to the interface is given by

$$S_{0,\xi} = -\phi gh\frac{\partial z_\mathrm{b}}{\partial \xi} + g\frac{h^2}{2}\frac{\partial \phi}{\partial \xi} \tag{10}$$

In the proposed approach the flux is estimated using a Harten-Lax-van Leer (HLL) Riemann solver [17, 18]. The source term must be discretized in such a way that steady-state conditions are satisfied. Therefore, the discretization of the source term is conditioned by the Riemann solver used. However, the method presented here can be applied for any choice of Riemann solver.

The HLL Riemann solver is based on the assumption of two discontinuities travelling at speeds λ^- and λ^+ from the location of the initial discontinuity between the initial states $\mathbf{U}_\mathrm{L}$ and $\mathbf{U}_\mathrm{R}$. The solution between the two waves λ^- and λ^+ is approximated by a constant state

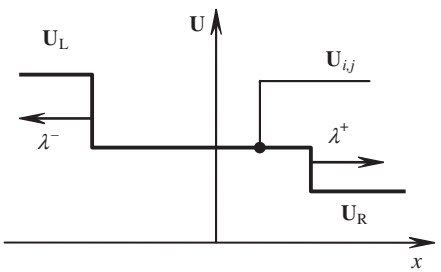

Figure 2. Definition sketch for the HLL Riemann solver. The solution is approximated by a region of constant state $\mathbf{U}_{i,j}$ separated from the left and right states of the Riemann problem by two discontinuities moving at speeds λ^- and λ^+.

(Figure 2). Applying the Rankine–Hugoniot conditions across these discontinuities leads to the following estimate:

$$(\phi\mathbf{F})_{i,j} \cong \frac{1}{\lambda^+ - \lambda^-}[\lambda^+\phi_L\mathbf{F}(\mathbf{U}_L) - \lambda^-\phi_R\mathbf{F}(\mathbf{U}_R) + \lambda^-\lambda^+(\phi_R\mathbf{U}_R - \phi_L\mathbf{U}_L)] \tag{11}$$

The wave celerities are estimated as in Reference [22]

$$\begin{aligned} \lambda^- &= \min(u_L - c_L, u_R - c_R, 0) \\ \lambda^+ &= \max(u_L + c_L, u_R + c_R, 0) \end{aligned} \tag{12}$$

the min and max operators allowing the validity of Equation (11) to be extended to super-critical conditions. Also note that Equation (12) is used only for the determination of the first two components of $\mathbf{F}$, the third component of $\mathbf{F}$ being calculated using the velocity u (that is, the propagation speed of the contact discontinuity in v) so as to minimize numerical diffusion

$$\begin{aligned} \lambda^- &= \min(u_{i,j}, 0) \\ \lambda^+ &= \max(u_{i,j}, 0) \end{aligned} \tag{13}$$

In order to ensure equilibrium under steady state conditions the expressions of $\mathbf{U}$ and $S_{0,\xi}$ are slightly modified by introducing the elevation z of the free-surface

$$z = z_b + h \tag{14}$$

where z_b is the bottom elevation. Following the idea developed in Reference [13], $\mathbf{U}$ is redefined as

$$\mathbf{U} = \begin{bmatrix} z \\ hu_x \\ hu_y \end{bmatrix} \tag{15}$$

and the source term $S_{0,\xi}$ is redefined as follows:

$$S_{0,\xi} = -g\phi h\frac{\partial}{\partial\xi}(z - h) + \frac{g}{2}h^2\frac{\partial\phi}{\partial\xi}$$

$$= -g\phi h\frac{\partial z}{\partial \xi} + g\phi h\frac{\partial h}{\partial \xi} + \frac{g}{2}h^2\frac{\partial \phi}{\partial \xi}$$

$$= -g\phi h\frac{\partial z}{\partial \xi} + \frac{g}{2}\frac{\partial}{\partial \xi}(\phi h^2) \tag{16}$$

Using $\partial z/\partial \xi$ instead of $\partial z_b/\partial \xi$ in the expression of $S_{0,\xi}$ prevents spurious source term from arising when the water is at rest on an irregular topography. Details about these modifications are given in Sections 3.2 and 3.3.

3.2. *Computation of the mass flux*

The mass flux is obtained from the first component of the vector equation (11)

$$(\phi hu)_{i,j} \cong \frac{1}{\lambda^+ - \lambda^-}\{\lambda^+(\phi uh)_L - \lambda^-(\phi uh)_R + \lambda^-\lambda^+[(\phi z)_R - (\phi z)_L]\} \tag{17}$$

Equation (17) satisfies the equilibrium condition when ϕ is identical on both sides of the interface. This is easily checked for the case of water at rest, where $z_L = z_R$ and $u_L = u_R = 0$. If $\phi_L = \phi_R$, a zero mass flux is obtained thanks to the modification (15) derived from the arguments developed in References [23, 13]. Indeed, if the bottom level is not constant, using h instead of z in Equation (17) yields a non-zero discharge at the interface because h_L and h_R are different. Spurious oscillations appear in the free surface and propagate throughout the entire calculation. Using z instead of h as a conserved variable in the continuity equation allows this drawback to be eliminated. However, this modification is not sufficient in situations where the porosity varies across the interface. Indeed, if $z_L = z_R$ and $u_L = u_R = 0$, inserting the condition $\phi_L \neq \phi_R$ into Equation (17) yields a non-zero mass flux. A possible modification of Equation (17) could be to multiply the difference $z_R - z_L$ by an average value ϕ_{LR} (to be determined) of the porosity between the cells L and R

$$(\phi hu)_{i,j} \cong \frac{1}{\lambda^+ - \lambda^-}[\lambda^+(\phi uh)_L - \lambda^-(\phi uh)_R + \lambda^-\lambda^+(z_R - z_L)\phi_{LR}] \tag{18}$$

However, this formulation is not satisfactory because it does not yield realistic steady-state conditions when the discharge is non-zero in the presence of a porosity gradient. Consider the following steady-state situation:

$$\left.\begin{aligned} \phi_L \neq \phi_R \\ (\phi hu)_L = (\phi hu)_R = \quad q \end{aligned}\right\} \tag{19}$$

with $q \neq 0$. Steady-state continuity imposes that $(\phi hu)_{i,j}$ should be equal to q. Substituting this condition and Equation (19) into Equation (18) leads to the necessary condition

$$z_L = z_R \tag{20}$$

Equation (20) is not physically acceptable because it does not allow the momentum equation to be satisfied when $q \neq 0$. In the case of a non-zero discharge the gradient in the momentum flux ϕhu^2 should be balanced by a gradient in the hydrostatic pressure term $\phi gh^2/2$.

Consequently, z_L and z_R should be different. The following expression is proposed:

$$(\phi hu)_{i,j} \cong \frac{\phi_{LR}}{\lambda^+ - \lambda^-}[\lambda^+(uh)_L - \lambda^-(uh)_R + \lambda^-\lambda^+(z_R - z_L)] \tag{21}$$

where ϕ_{LR} is approximated as follows:

$$\phi_{LR} \cong \min(\phi_L, \phi_R) \tag{22}$$

This estimate is based on the consideration that the mass exchange is driven by the narrower of the two sections. It has the additional advantage that it accounts automatically for the fact that water cannot flow into a region of zero porosity because in such a case the following condition is automatically satisfied:

$$\phi_{LR} = 0 \quad \text{if} \quad \min(\phi_L, \phi_R) = 0 \tag{23}$$

3.3. Computation of the longitudinal momentum flux and source terms

The momentum flux in the direction ξ is given by the second component of the vector equation (11)

$$(\phi hu^2)_{i,j} \cong \frac{1}{\lambda^+ - \lambda^-}\left\{\lambda^+\left(\phi hu^2 + \frac{g}{2}\phi h^2\right)_L - \lambda^-\left(\phi hu^2 + \frac{g}{2}\phi h^2\right)_R + \lambda^-\lambda^+[(\phi hu)_R - (\phi hu)_L]\right\} \tag{24}$$

The integral $\Delta S_{0,\xi}$ of the source term $S_{0,\xi}$ across the interface is written in the form

$$\Delta S_{0,\xi} = -g(\phi h)_{i,j}(z_R - z_L) + \frac{g}{2}[(\phi h^2)_R - (\phi h^2)_L] \tag{25}$$

where $(\phi h)_{i,j}$ is estimated in such a way that the steady state conditions are satisfied for any value of q.

The estimate of $(\phi h)_{i,j}$ is derived by writing the mass and momentum balance on the control volume formed by the cells i and j. For the sake of simplicity the necessary condition for the expression of $(\phi h)_{i,j}$ is derived for a flat bottom. In such a case the difference $(z_R - z_L)$ can be replaced with the difference $(h_R - h_L)$ and Equation (25) becomes

$$\Delta S_{0,\xi} = -g(\phi h)_{i,j}(h_R - h_L) + \frac{g}{2}[(\phi h^2)_R - (\phi h^2)_L] \tag{26}$$

The estimate of $(\phi h)_{i,j}$ must be such that the equilibrium condition over the cells i and j is satisfied. Writing the discrete mass and momentum balance over the domain formed by the cells i and j gives

$$\left(\phi hu^2 + \frac{g}{2}h^2\right)_L - \left(\phi hu^2 + \frac{g}{2}h^2\right)_R + \Delta S_{0,\xi} = 0 \tag{27}$$

Substituting Equation (26) into Equation (27) leads to the following relationship:

$$(\phi hu^2)_L - (\phi hu^2)_R - g(\phi h)_{i,j}(h_R - h_L) = 0 \tag{28}$$

Substituting Equation (19) into Equation (28) yields the equality

$$(u_{\mathrm{L}} - u_{\mathrm{R}})q - g(\phi h)_{i,j}(h_{\mathrm{R}} - h_{\mathrm{L}}) = 0 \tag{29}$$

Equation (29) is the momentum balance obtained using the discrete estimates (24) and (26) of the flux and the source term, respectively. The expression of $(\phi h)_{i,j}$ is obtained by comparing Equation (29) to the analytical momentum balance over the same control volume (represented in Figure 3 for the case $\phi_{\mathrm{L}} \geqslant \phi_{\mathrm{R}}$). For the sake of clarity the section available to the flow on each side of the interface has been lumped into a single region of width ϕw in the figure. The momentum flux M_{AB} entering the control volume by the left-hand boundary [AB] of the control volume is given by

$$M_{\mathrm{AB}} = q u_{\mathrm{L}} w_{i,j} \tag{30}$$

The momentum flux M_{CD} leaving the control volume by the right-hand edge [CD] is given by

$$M_{\mathrm{CD}} = q u_{\mathrm{R}} w_{i,j} \tag{31}$$

The pressure forces exerted on the edges [AB], [CD] and [EF] are given by

$$\begin{aligned} P_{\mathrm{AB}} &= \frac{g}{2}\phi_{\mathrm{L}} h_{\mathrm{L}}^2 w_{i,j} \\ P_{\mathrm{CD}} &= \frac{g}{2}\phi_{\mathrm{R}} h_{\mathrm{R}}^2 w_{i,j} \\ P_{\mathrm{EF}} &= \frac{g}{2}(\phi_{\mathrm{L}} - \phi_{\mathrm{R}}) h_{\mathrm{L}}^2 w_{i,j} \end{aligned} \tag{32}$$

Balancing the momentum fluxes and the pressure forces yields

$$M_{\mathrm{AB}} - M_{\mathrm{CD}} + P_{\mathrm{AB}} - P_{\mathrm{CD}} - P_{\mathrm{EF}} = 0 \tag{33}$$

Substituting Equations (30)–(32) into Equation (33) and dividing by $w_{i,j}$ leads to

$$(u_{\mathrm{L}} - u_{\mathrm{R}})q + \frac{g}{2}[(\phi_{\mathrm{L}} h_{\mathrm{L}}^2 - \phi_{\mathrm{R}} h_{\mathrm{R}}^2) + (\phi_{\mathrm{R}} - \phi_{\mathrm{L}}) h_{\mathrm{L}}^2] = 0 \quad \text{if} \quad \phi_{\mathrm{L}} \geqslant \phi_{\mathrm{R}} \tag{34}$$

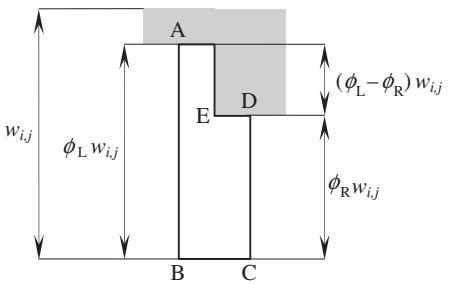

Figure 3. Plan view sketch for momentum balance across an interface with different porosities on the left- and right-hand sides (here for $\phi_{\mathrm{L}} > \phi_{\mathrm{R}}$).

A similar reasoning for the case $\phi_L \leqslant \phi_L$ leads to the following relationship:

$$(u_L - u_R)q + \frac{g}{2}[(\phi_L h_L^2 - \phi_R h_R^2) + (\phi_L - \phi_R)h_R^2] = 0 \quad \text{if} \quad \phi_L \leqslant \phi_R \tag{35}$$

where q denotes the steady-state unit discharge. Note that Equations (34) and (35) can be rewritten in condensed form as

$$\begin{aligned}(u_L - u_R)q + \frac{g}{2}\{(\phi_L h_L^2 - \phi_R h_R^2) + [\min(\phi_R, \phi_L) - \phi_L]h_L^2 \\ -[\min(\phi_R, \phi_L) - \phi_R]h_R^2\} = 0\end{aligned} \tag{36}$$

Equation (29) is equivalent to Equation (36) only if

$$\begin{aligned}(\phi h)_{i,j}(h_R - h_L) = \tfrac{1}{2}\{(\phi_R h_R^2 - \phi_L h_L^2) - [\min(\phi_L, \phi_R) - \phi_L]h_L^2 \\ +[\min(\phi_L, \phi_R) - \phi_R]h_R^2\}\end{aligned} \tag{37}$$

Equation (37) can be written as

$$(\phi h)_{i,j}(h_R - h_L) = \begin{cases} \tfrac{1}{2}[(\phi_R h_R^2 - \phi_L h_L^2) + (\phi_L - \phi_R)h_L^2] & \text{if} \quad \phi_L \geqslant \phi_R \\ \tfrac{1}{2}[(\phi_R h_R^2 - \phi_L h_L^2) + (\phi_L - \phi_R)h_R^2] & \text{if} \quad \phi_L \leqslant \phi_R \end{cases} \tag{38}$$

Equation (38) can be simplified into

$$(\phi h)_{i,j} = \begin{cases} \dfrac{(h_R + h_L)}{2}\phi_R & \text{if} \quad \phi_L \geqslant \phi_R \\ \dfrac{(h_R + h_L)}{2}\phi_L & \text{if} \quad \phi_L \leqslant \phi_R \end{cases} \tag{39}$$

Equation (39) is rewritten as

$$(\phi h)_{i,j} = \frac{h_L + h_R}{2}\min(\phi_L, \phi_R) \tag{40}$$

From a practical point of view the source term over cell i in Equation (6) is computed as the sum of the contributions of the source terms across each cell interface. Each component of this sum is treated in an upwind fashion [10]. This results in the following modified form of Equation (6), adapted to cell i and cell j on the left- and right-hand side of the interface, respectively,

$$\begin{aligned}\mathbf{U}_i^{n+1} &= \mathbf{U}_i^n - \frac{\Delta t}{\phi_i}\sum_{j\in N(i)}\mathbf{P}_{i,j}\left[\frac{w_{i,j}}{A_i}(\phi\mathbf{F})_{i,j}^{n+1/2} + (\mathbf{S}_i)_{i,j}^{n+1/2}\right] \\ \mathbf{U}_j^{n+1} &= \mathbf{U}_j^n + \frac{\Delta t}{\phi_j}\sum_{j\in N(i)}\mathbf{P}_{i,j}\left[\frac{w_{i,j}}{A_j}(\phi\mathbf{F})_{i,j}^{n+1/2} + (\mathbf{S}_j)_{i,j}^{n+1/2}\right]\end{aligned} \tag{41}$$

where the source term $(\mathbf{S}_i)_{i,j}^{n+1/2}$ is estimated as

$$(S_i)_{i,j}^{n+1/2} = \frac{-\lambda^-}{\lambda^+ - \lambda^-} \frac{w_{i,j}}{A_i} \Delta S_{0,\xi} \tag{42}$$

where $\Delta S_{0,\xi}$ is computed according to Equations (25) and (40). Conversely, the contribution of the bottom and porosity source term to the momentum equation in the cell j is given by

$$(S_j)_{i,j}^{n+1/2} = \frac{\lambda^+}{\lambda^+ - \lambda^-} \frac{w_{i,j}}{A_j} \Delta S_{0,\xi} \tag{43}$$

3.4. Computation of the transverse momentum flux

The transverse momentum flux is given by the third component of the vector equation (11). If the velocity at the interface is positive the momentum flux must be computed using the value v_{L}. Otherwise the value v_{R} must be used. The following formula accounts for both situations:

$$(\phi huv)_{i,j} \cong \frac{(\phi uh)_{i,j} + |(\phi uh)_{i,j}|}{2} v_{\mathrm{L}} + \frac{(\phi uh)_{i,j} - |(\phi uh)_{i,j}|}{2} v_{\mathrm{R}} \tag{44}$$

3.5. Computation of the friction source term

The friction source term is discretized in the global coordinate system (x, y) using a time splitting procedure. Treating the friction terms separately from the other terms leads to the following system of coupled Ordinary Differential Equations (ODEs):

$$\frac{\mathrm{d}(\phi h)}{\mathrm{d}t} = 0 \tag{45a}$$

$$\frac{\mathrm{d}(\phi h u_x)}{\mathrm{d}t} = -\left(\frac{1}{K^2 h^{4/3}} + s_x\right)(u_x^2 + u_y^2)^{1/2} \phi g h u_x \tag{45b}$$

$$\frac{\mathrm{d}(\phi h u_y)}{\mathrm{d}t} = -\left(\frac{1}{K^2 h^{4/3}} + s_y\right)(u_x^2 + u_y^2)^{1/2} \phi g h u_y \tag{45c}$$

Substituting Equation (45a) into Equations (45b)–(45c) and dividing by ϕh leads to

$$\frac{\mathrm{d}u_x}{\mathrm{d}t} = -\left(\frac{1}{K^2 h^{7/3}} + s_x\right)(u_x^2 + u_y^2)^{1/2} g u_x \tag{46a}$$

$$\frac{\mathrm{d}u_y}{\mathrm{d}t} = -\left(\frac{1}{K^2 h^{7/3}} + s_y\right)(u_x^2 + u_y^2)^{1/2} g u_y \tag{46b}$$

The coupled Ordinary Differential Equations (46a)–(46b) are semi-discretized over each cell i using the following explicit linearization that allows the coupling between u and v to be

broken:

$$\frac{\mathrm{d}u_x}{\mathrm{d}t} = -\left(\frac{1}{K^2 h_i^{n^{7/3}}} + s_x\right)\left[(u_x^2)_i^n + (u_y^2)_i^n\right]^{1/2} g u_x \tag{47a}$$

$$\frac{\mathrm{d}u_y}{\mathrm{d}t} = -\left(\frac{1}{K^2 h_i^{n^{7/3}}} + s_y\right)\left[(u_x^2)_i^n + (u_y^2)_i^n\right]^{1/2} g u_y \tag{47b}$$

Equations (47) have the following analytical solution:

$$\begin{aligned} u_{x_i}^{n+1} &= \exp\left[-\left(\frac{\left[(u_x^2)_i^n + (u_y^2)_i^n\right]^{1/2}}{K^2 h_i^{n^{7/3}}} + s_x\right) g\Delta t\right] u_{x_i}^n \\ u_{y_i}^{n+1} &= \exp\left[-\left(\frac{\left[(u_x^2)_i^n + (u_y^2)_i^n\right]^{1/2}}{K^2 h_i^{n^{7/3}}} + s_y\right) g\Delta t\right] u_{y_i}^n \end{aligned} \tag{48}$$

It is recalled that s_x and s_y accounts for an additional head loss due to urban singularities (see Appendix B for the details of the derivation).

3.6. Stability constraint

The numerical scheme being explicit, it is subject to a stability constraint that yields a maximum permissible computational time step. The maximum permissible time step is such that the sum of the areas of the domain of dependence of the interfaces of each given cell should not exceed the area of this cell. This criterion has proved to preclude instabilities from appearing even in the case of an overlap of the domains of dependence of the interfaces when the flow is strongly divergent [24]. The area $A_{i,j}$ of the domain of dependence of an interface (i, j) is bounded by the following quantity:

$$A_{i,j} \leqslant w_{i,j}\Delta t \max\left\{\left[(u_x^2)_i^n + (u_y^2)_i^n\right]^{1/2} + c_i^n, \left[(u_x^2)_j^n + (u_y^2)_j^n\right]^{1/2} + c_j^n\right\} \tag{49}$$

where the quantity between accolades is an upper bound for the speed of the fastest characteristic issued from the interface. The time step should be such that

$$\sum_{j\in N(i)} A_{i,j} \leqslant A_i \quad \text{for all } i \tag{50}$$

A sufficient condition for Equation (50) to be satisfied given the relationship (49) is that the maximum permissible time step $\Delta t_{\max}$ be defined as

$$\Delta t_{\max} = \min_i \frac{A_i}{\sum_{j\in N(i)} w_{i,j} \max\left\{\left[(u_x^2)_i^n + (u_y^2)_i^n\right]^{1/2} + c_i^n, \left[(u_x^2)_j^n + (u_y^2)_j^n\right]^{1/2} + c_j^n\right\}} \tag{51}$$

Note that in the case of a rectangular grid the condition reduces to the standard one-dimensional Courant–Friedrichs–Lewy condition that the sum of the Courant numbers in each direction of space should not exceed unity.

4. COMPUTATIONAL EXAMPLES

Two types of computational examples are provided in the present section. The first type of example consists of analytical test cases where the quality of the numerical solution is assessed via a comparison with analytical or semi-analytical solutions. Such tests are described in Sections 4.1–4.3. The analytical test cases presented in Sections 4.1–4.3 are derived from classical problems encountered in the shallow water literature but differ from these in that a variable porosity is introduced into the equations. Sections 4.1 and 4.2 deal with one-dimensional problems. Section 4.3 deals with a two-dimensional problem. The second type of example allows the validity of the modified shallow water equations to be assessed by comparing the model results with experimental data. This is the subject of Section 4.4.

4.1. One-dimensional dambreak with variable porosity

The first computational example consists of a one-dimensional dambreak simulation over a flat bottom with a porosity varying from 0 at the left-hand boundary of the domain to 1 at the right-hand boundary. The parameters of the test case are given in Table I. Note that under the assumption of a one-dimensional behaviour and a linearly varying porosity Equation (1) becomes

$$\frac{\partial}{\partial t}(\phi_x x\mathbf{U}) + \frac{\partial}{\partial x}(\phi_x x\mathbf{F}) = \mathbf{S} \tag{52}$$

where $\phi x = \mathrm{d}\phi/\mathrm{d}x$ is a constant. The momentum source term $S_{0,x}$ reduces to

$$S_{0,x} = \phi_x g\frac{h^2}{2} \tag{53}$$

Dividing Equations (52)–(53) by ϕ_x leads to the expression of the classical shallow water equations in cylindrical coordinates, where x now plays the role of the radial coordinate. The one-dimensional problem is therefore equivalent to a circular dambreak problem with a uniform porosity. The radius of the dam is equal to x_0 and the water depths inside and outside the circular region are given by $h_{0,\mathrm{L}}$ and $h_{0,\mathrm{R}}$, respectively. Figures 4–9 compare the numerical solution of the variable porosity problem to the reference solution obtained solving the circular dambreak problem with a uniform porosity. The circular dambreak problem used a reference solution is solved over a refined grid of cell width $\Delta x = 10^{-4}$ m. The convergence of the reference solution was checked by carrying out simulations on grids with a decreasing

Table I. Parameters of the one-dimensional dambreak test case with variable porosity.

Symbol	Meaning	Value
g	Gravitational acceleration	$9.81\,\mathrm{m}^2/\mathrm{s}$
$h_{0,\mathrm{L}}$	Initial water depth on the left-hand side of the dam	10 m
$h_{0,\mathrm{R}}$	Initial water depth on the right-hand side of the dam	1 m
L	Length of the domain	100 m
x_0	Location of the dam	50 m
Δx	Cell size	1 m, 0.1 m, 0.01 m
ϕ_x	Radial derivative of the porosity	0.1/m

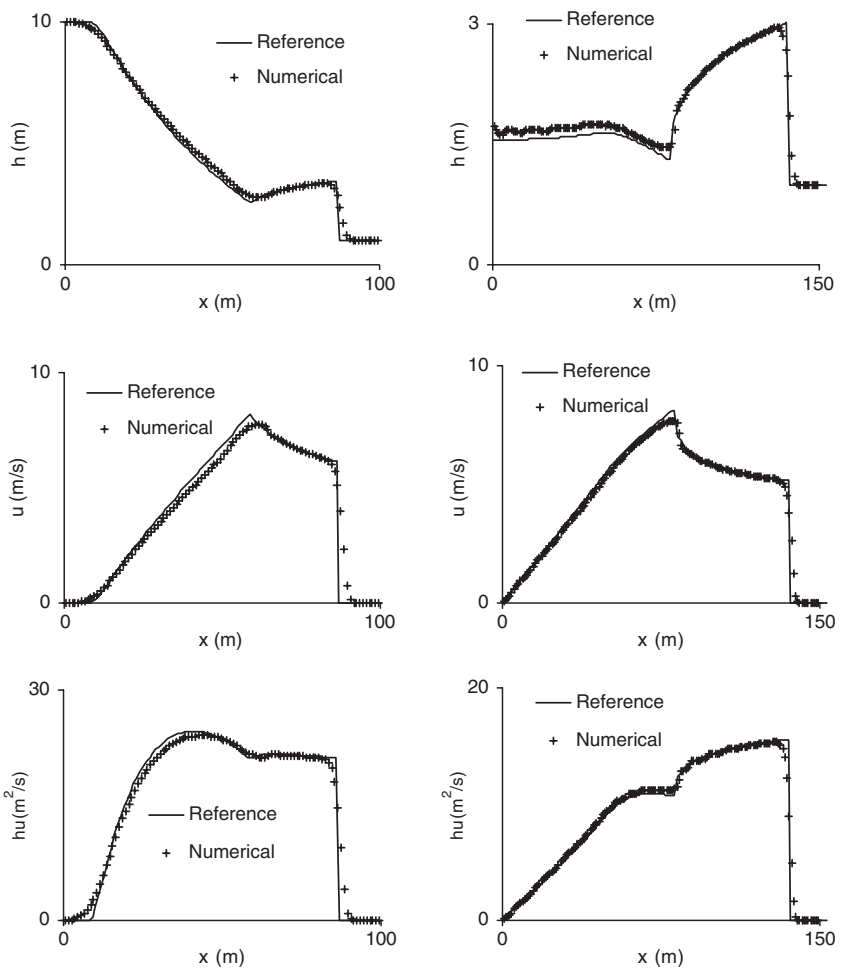

Figure 4. One-dimensional dambreak problem with variable porosity. Reference and numerical solutions at $t = 4$ s (left) and $t = 10$ s (right) for a cell width $\Delta x = 1$ m and a computational time step $\Delta t = 2.2 \times 10^{-2}$ s.

cell width. No significant difference being detected between the solutions obtained for cell widths $\Delta x = 10^{-3}$ and 10^{-4} m, the solution for $\Delta x = 10^{-4}$ m is considered as converged.

Figure 4 shows the profiles obtained using the second-order MUSCL reconstruction at $t = 4$ and 10 s for a cell width $\Delta x = 1$ m and a time step $\Delta t = 2.2 \times 10^{-2}$ s that corresponds to the maximum permissible time step. Figure 5 shows the profiles obtained for the same cell size and a time step $\Delta t = 10^{-3}$ s. Figures 6 and 7 represent the same profiles as do Figures 3 and 4, respectively, with both Δx and Δt divided by 10. Figures 8 and 9 present the results for a cell size and time step 100 times as small as in Figures 4 and 5. The numerical solution can be seen to converge to the semi-analytical solution when both the cell size and time step are reduced.

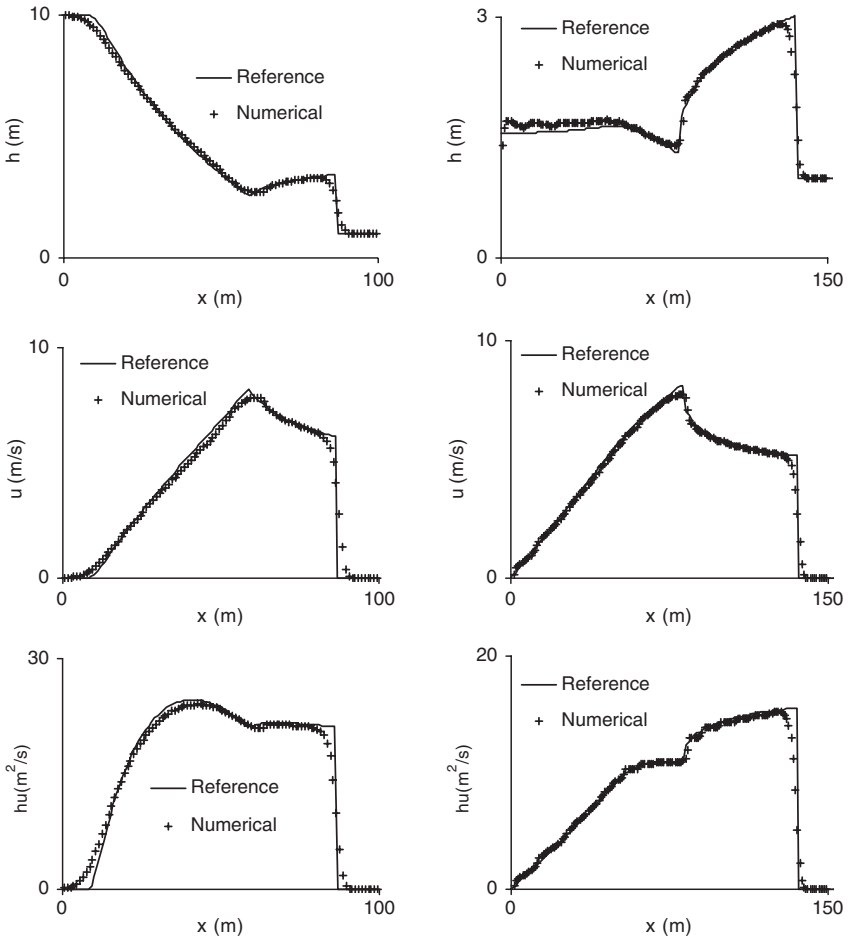

Figure 5. One-dimensional dambreak problem with variable porosity. Reference and numerical solutions at $t = 4$ s (left) and $t = 10$ s (right) for a cell width $\Delta x = 1$ m and a computational time step $\Delta t = 10^{-3}$ s.

4.2. *One-dimensional dambreak across a porosity discontinuity*

The second computational example consists of a one-dimensional dambreak simulation across a porosity discontinuity. In this test the porosity is equal to unity on the upstream side of the dam and is smaller on the downstream side of the dam. The parameters of the test case are given in Table II. The discontinuity in the value of the porosity at x_0 leads to a reduction in the exchange section between the upstream and downstream sides. Therefore, the structure of the solution of this problem is different from that of the classical dambreak problem. The part of the solution located to the right of the discontinuity has the same structure as the solution of the classical dambreak problem, where a region of constant state is connected to the right state of the Riemann problem by a shock wave and to the location of the initial discontinuity

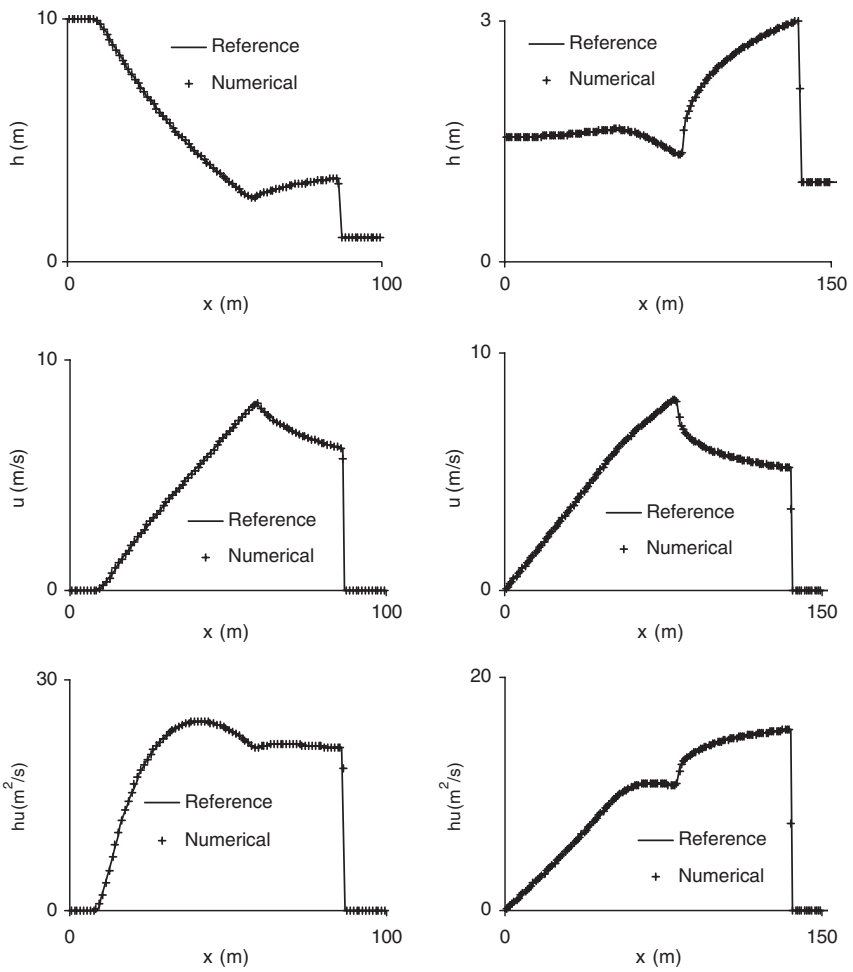

Figure 6. One-dimensional dambreak problem with variable porosity. Reference and numerical solutions at $t = 4\,\mathrm{s}$ (left) and $t = 10\,\mathrm{s}$ (right) for a cell width $\Delta x = 0.1\,\mathrm{m}$ and a time step $\Delta t = 2.2 \times 10^{-3}\,\mathrm{s}$.

by a rarefaction wave. In contrast with the classical dambreak problem, the rarefaction wave does not spread on the left-hand side of the discontinuity because the porosity is larger there, leading to a reduced flow velocity. The region located immediately to the left of the discontinuity is therefore a region of constant state, connected to the left state of the Riemann problem by a rarefaction wave travelling to the left (Figure 10). The values $\mathbf{U}_1$ and $\mathbf{U}_2$ in the regions of constant state can be determined by solving the following system of equations:

$$u_{\mathrm{L}} + 2(gh_{\mathrm{L}})^{1/2} = u_1 + 2(gh_1)^{1/2} \tag{54a}$$

$$\phi_{\mathrm{L}} h_1 u_1 = \phi_{\mathrm{R}} h_d u_d \tag{54b}$$

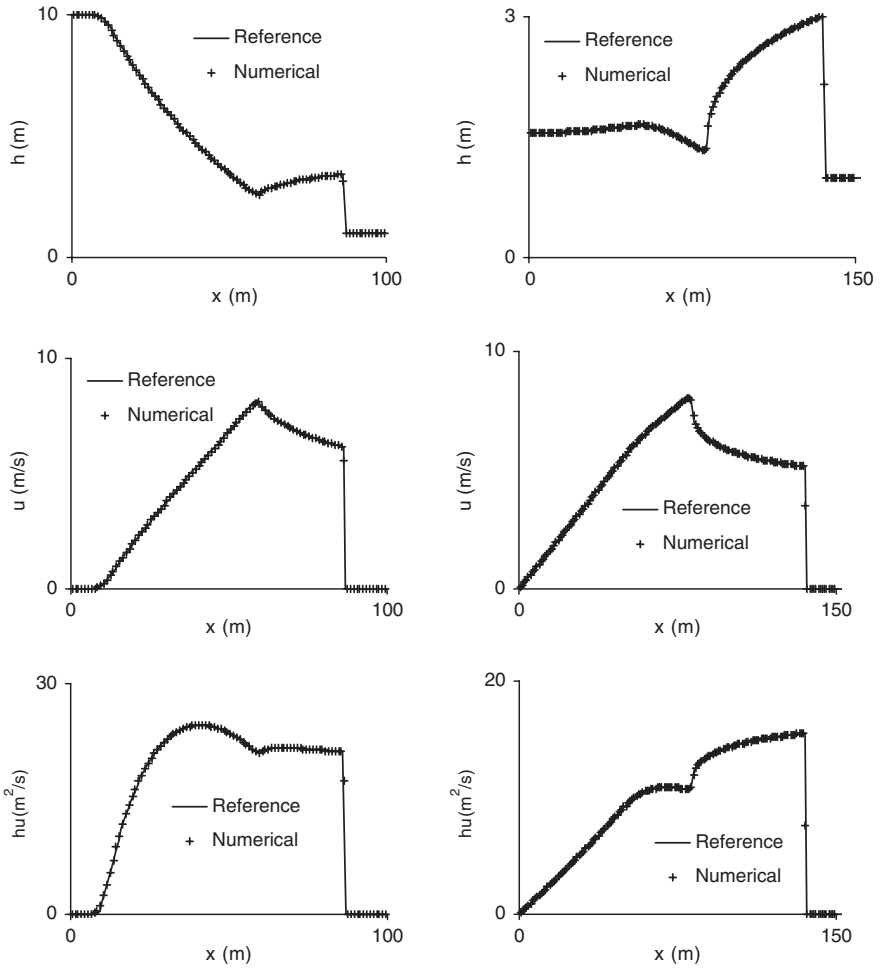

Figure 7. One-dimensional dambreak problem with variable porosity. Reference and numerical solutions at $t = 4\,\mathrm{s}$ (left) and $t = 10\,\mathrm{s}$ (right) for a cell width $\Delta x = 0.1\,\mathrm{m}$ and a time step $\Delta t = 10^{-4}\,\mathrm{s}$.

$$\phi_{\mathrm{L}}\left(h_1 u_1^2 + \frac{g}{2}h_1^2\right) = \phi_{\mathrm{R}}\left(h_d u_d^2 + \frac{g}{2}h_d^2\right) \tag{54c}$$

$$u_d + 2(gh_d)^{1/2} = u_1 + 2(gh_2)^{1/2} \tag{54d}$$

$$u_d - (gh_d)^{1/2} = 0 \tag{54e}$$

$$(h_2 - h_{\mathrm{R}})s = h_2 u_2 - h_{\mathrm{R}} u_{\mathrm{R}} \tag{54f}$$

$$h_1 u_1 s = h_1 u_1^2 + \frac{g}{2}(h_1^2 - h_2^2) \tag{54g}$$

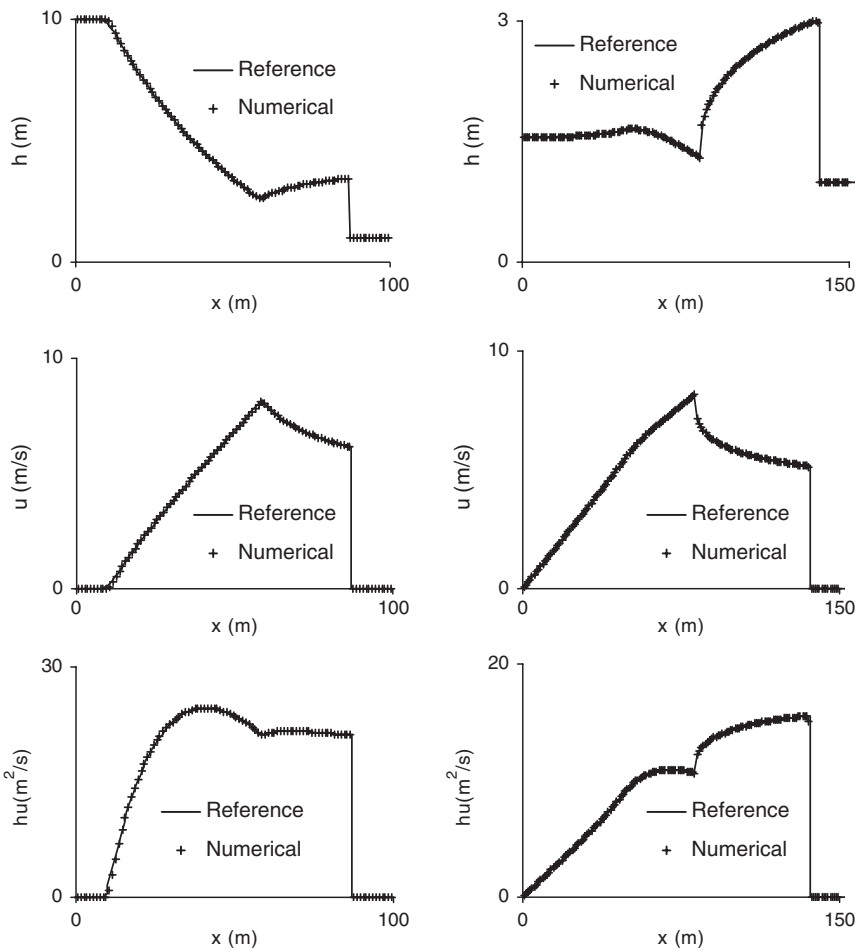

Figure 8. One-dimensional dambreak problem with variable porosity. Reference and numerical solutions at $t = 4$ s (left) and $t = 10$ s (right) for a cell width $\Delta x = 0.01$ m and a time step $\Delta t = 2.2 \times 10^{-4}$ s.

where s is the propagation speed of the shock, and h_d and u_d denote the water depth and the velocity, respectively, on the right-hand side of the porosity discontinuity. Equation (54a) expresses the invariance of the quantity $u + 2(gh)^{1/2}$ across the rarefaction wave heading to the left. Equations (54b)–(54c) express mass and momentum conservation across the porosity discontinuity. Equation (54d) expresses the invariance of the quantity $u + 2(gh)^{1/2}$ across the rarefaction wave issued from the porosity discontinuity and Equation (54e) states critical conditions at the discontinuity. Equations (54f)–(54g) express mass and momentum conservation across the shock. Solving Equations (54a)–(54g) for h_1, u_1, h_2, u_2, h_d, u_d and s allows the solution to be determined uniquely. In the present case the solution was obtained using a Newton–Raphson procedure. Figure 11 gives a comparison of the numerical and analytical

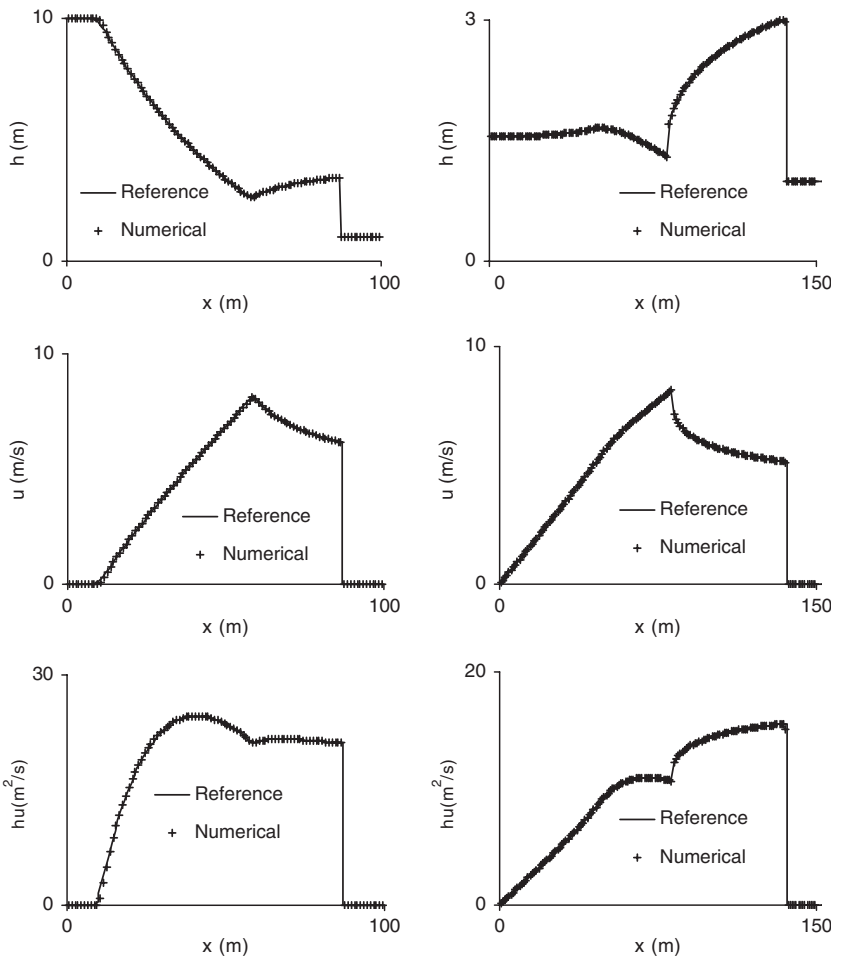

Figure 9. One-dimensional dambreak problem with variable porosity. Reference and numerical solutions at $t = 4\,\mathrm{s}$ (left) and $t = 10\,\mathrm{s}$ (right) for a cell width $\Delta x = 0.01\,\mathrm{m}$ and a time step $\Delta t = 10^{-5}\,\mathrm{s}$.

profiles for a cell width $\Delta x = 1\,\mathrm{m}$ and computational time steps $\Delta t = 10^{-3}$ and $2.7 \times 10^{-4}\,\mathrm{s}$. The latter value of the time step corresponds to the maximum permissible value allowed by the stability constraint. Figure 12 compares the analytical solution and the numerical solution obtained using a cell width $\Delta x = 0.1\,\mathrm{m}$ and time steps $\Delta t = 10^{-4}$ and $2.7 \times 10^{-3}\,\mathrm{s}$. As in the previous test, refining the mesh does not yield any significant improvement in the quality of the solution. In both cases a strong numerical diffusion appears across both the porosity discontinuity and the rarefaction wave, and both the unit discharge and the flow velocity appear to be slightly overestimated. Nevertheless, the propagation speeds of the various waves are computed correctly.

Table II. Parameters of the one-dimensional dambreak test case with porosity discontinuity.

Symbol	Meaning	Value
g	Gravitational acceleration	$9.81\,\mathrm{m}^2/\mathrm{s}$
$h_{0,\mathrm{L}}$	Initial water depth on the left-hand side of the dam	10 m
$h_{0,\mathrm{R}}$	Initial water depth on the right-hand side of the dam	1 m
L	Length of the domain	100 m
x_0	Location of the dam	50 m
Δx	Cell size	1 m, 0.1 m
ϕ_{L}	Porosity on the left-hand side of the dam	1
ϕ_{R}	Porosity on the right-hand side of the dam	0.5 and 0.1

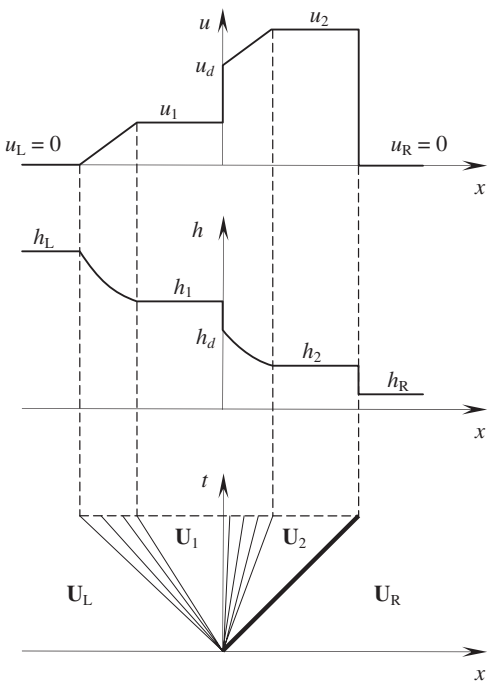

Figure 10. Structure of the analytical solution for the dambreak problem across a porosity discontinuity.

4.3. *Two-dimensional dambreak with variable porosity*

The third test case is a circular dambreak simulation where the porosity is variable in space. The porosity field is given by

$$\phi(x, y) = \frac{\phi_{\max}}{\max(r, r_0)} \qquad r = \frac{1}{[(x - x_0)^2 + (y - y_0)^2]^{1/2}} \tag{55}$$

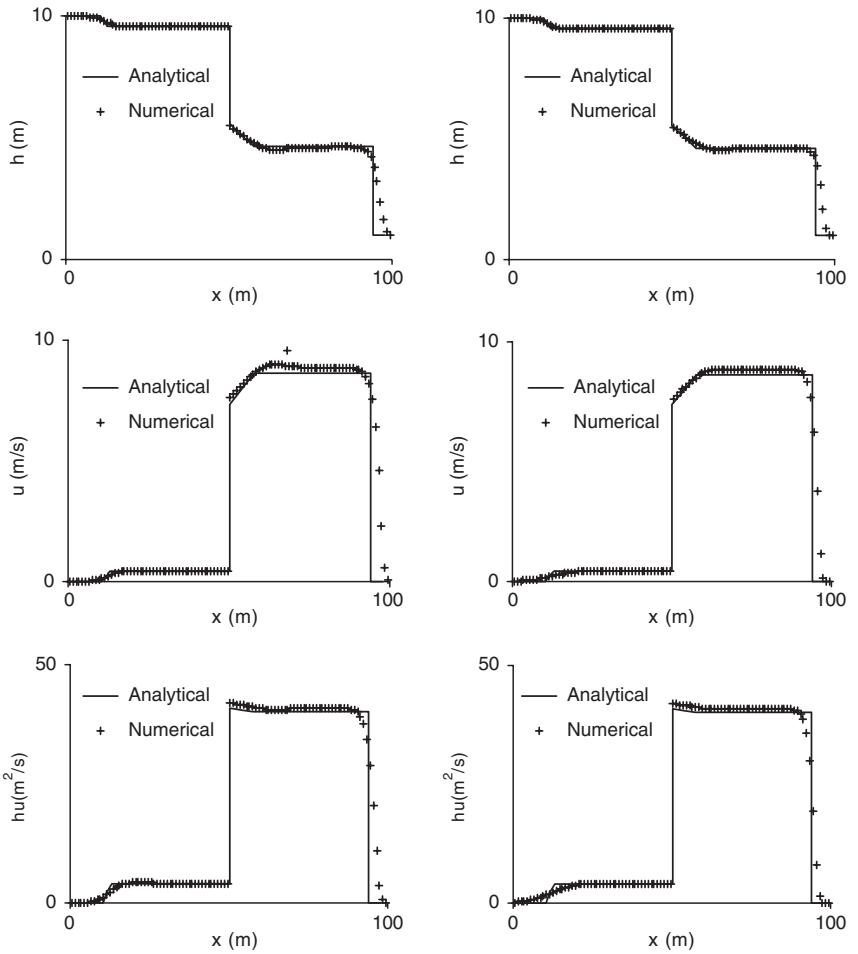

Figure 11. Dambreak problem across a porosity discontinuity. Results computed using a MUSCL reconstruction at $t = 4\,\mathrm{s}$ for a cell width $\Delta x = 1\,\mathrm{m}$ and a time step $\Delta t = 10^{-3}\,\mathrm{s}$ (left) and $\Delta t = 2.7 \times 10^{-2}\,\mathrm{s}$ (right).

where (x_0, y_0) are the coordinates of the centre of the dam. It is easy to check that substituting Equation (55) into the cylindrical version of Equation (1) leads to the classical one-dimensional shallow water equations. Therefore, the circular dambreak problem written in cylindrical coordinates with a porosity proportional to the inverse of the radial coordinate is equivalent to the one-dimensional dambreak problem with a constant porosity. The one-dimensional dambreak problem has an analytical solution [25]. The parameters of the test case are given in Table III. Figure 13 shows a perspective view of the computed water depths at $t = 4\,\mathrm{s}$. Figure 14 gives a comparison between the numerical and analytical solutions at $t = 4\,\mathrm{s}$, that is, shortly before the rarefaction wave reaches the centre of the dam, for a $1\,\mathrm{m} \times 1\,\mathrm{m}$ and a $0.25\,\mathrm{m} \times 0.25\,\mathrm{m}$ grid. The cross-sections plotted in Figure 14 is drawn along the main

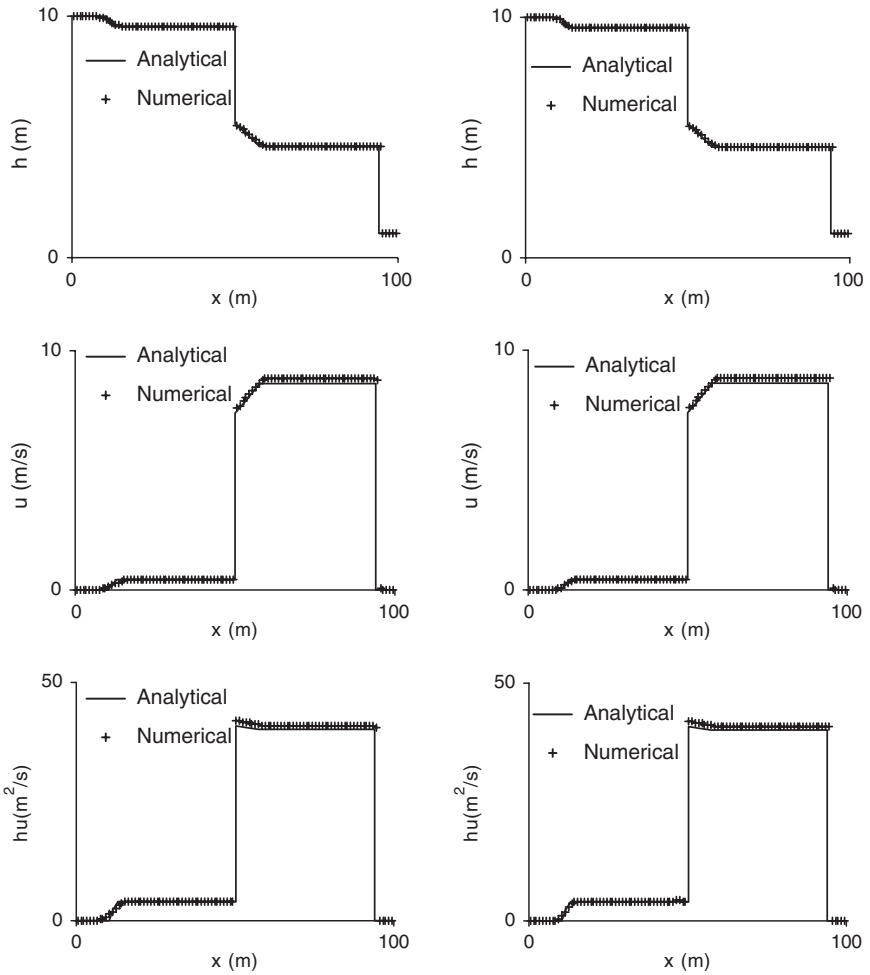

Figure 12. Dambreak problem across a porosity discontinuity. Results computed using a MUSCL reconstruction at $t = 4\,\mathrm{s}$ for a cell width $\Delta x = 0.1\,\mathrm{m}$ and a time step $\Delta t = 10^{-4}\,\mathrm{s}$ (left) and $\Delta t = 2.7 \times 10^{-3}\,\mathrm{s}$ (right).

direction of the grid. The differences between the profiles drawn along the grid diagonals and the main grid directions were found to be small. The behaviour of the numerical solution can be seen to converge to the analytical solution.

4.4. Toce test case

The purpose of this test case is to demonstrate the usefulness and the validity of the porous approach for the large scale modelling of floods in the presence of urbanized regions. The present subsection aims to show that a refined two-dimensional model may advantageously be replaced with a larger-scale model, based on a much coarser grid, where the urbanized area is

Table III. Parameters of the circular dambreak test case with variable.

Symbol	Meaning	Value
g	Gravitational acceleration	$9.81\,m^2/s$
$h_{0,L}$	Initial water depth on the left-hand side of the dam	10 m
$h_{0,R}$	Initial water depth on the right-hand side of the dam	1 m
L	Dimensions of the domain	200 m
r_0	Radius of the dam	50 m
x_0	x-coordinate of the centre of the dam	100 m
y_0	y-coordinate of the centre of the dam	100 m
Δx, Δy	Cell size in the x- and y-directions	1 m, 0.25 m
ϕ_{max}	Maximum value of the porosity in the domain	1

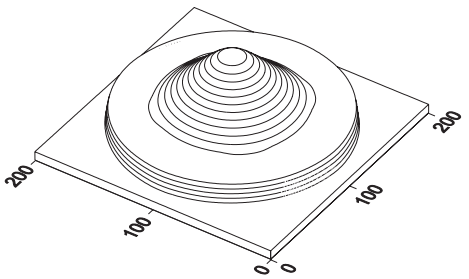

Figure 13. Circular dambreak problem with variable porosity. Perspective view of the computed water depth at $t = 4$ s.

represented using a reduced porosity. The test case was initially defined in the framework of the IMPACT European project [1]. It consists of experiments performed using a scale model of the Italian Toce valley at CESI (Italy). The model, the plan shape of which is roughly trapezoidal, is 7 m long and 3.5–5 m wide depending on the location. During the IMPACT experiments, square blocks were implemented in the scale model. Two configurations were tested during the project: aligned and staggered. The aligned configuration (Figure 15) is chosen for the present example because it is the least favourable configuration for a representation using the porous approach. Indeed, the presence of preferential flowpaths induced by the aligned blocks should be expected to be very difficult to represent using a porosity that reflects only a statistical property of the urban area. Two models were built. In the first model the grid is refined so as to provide a detailed discretization of the model geometry between the blocks (see detailed views of the computational grids in Figure 16). The equations solved in this model are the classical two-dimensional equations without porosity. The blocks are represented by impermeable boundaries. The second model uses a much coarser grid and solves the modified equations with porosity. In this model the rectangular area occupied by the blocks is characterized by a porosity smaller than unity. The values adopted for the porosity in this zone is the fraction of the cross-section available to the flow (that is, 4/9). The value of the Strickler coefficient was calibrated to be 60 all over the model. An additional head loss due to the singularities was incorporated in the urban area. The formulation retained is detailed

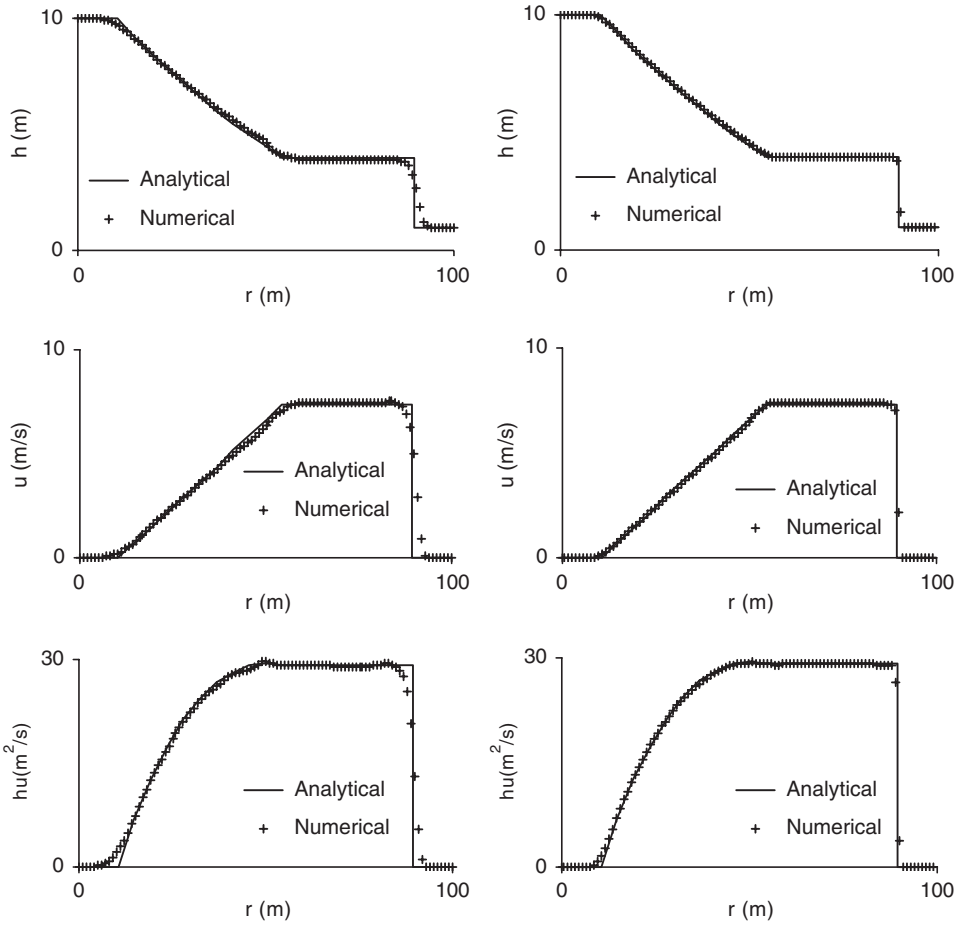

Figure 14. Circular dambreak problem with variable porosity. Analytical and numerical solutions obtained using a MUSCL reconstruction at $t = 4$ s for a cell width $\Delta x = 1$ m (left) and $\Delta x = 0.25$ m (right).

in Appendix B. The classical shallow water model and the model with porosity count 12 122 and 3226 cells, respectively. The numerical experiment consisted in simulating the effect of an input hydrograph used in one of the IMPACT experiments (Figure 17) at the upstream boundary of the model and comparing the simulation results given by both models. Figure 18 shows the free surface elevations and the unit discharges computed by the porosity model at $t = 20$ s. Two straight lines are defined, along which profiles of the computed free surface elevations are drawn. Profile 1 is located in the middle of one of the 'streets' between the blocks. Profile 2 is aligned with the centres of the square blocks. Figure 19 gives a comparison of the computed free surface elevations along these two profiles. Quite expectedly, the free-surface elevation computed by the refined and coarse models are different in the region occupied by the blocks (i.e. the part of the profile located between the points A and B). In

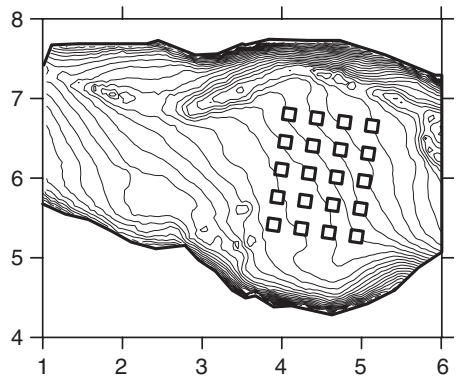

Figure 15. Topography of the valley for the Toce test case. Locations of the square blocks in the aligned configuration. Contour line spacing 0.005 m.

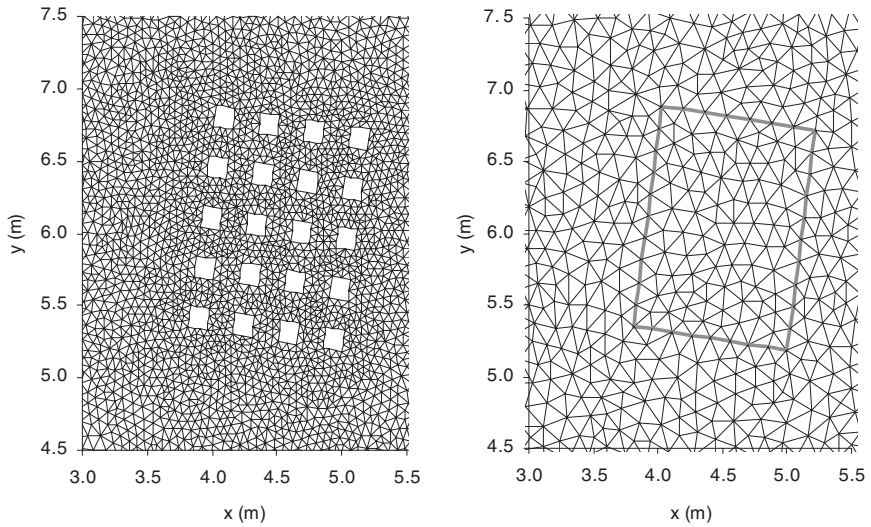

Figure 16. Detailed view of the mesh in the aligned configuration for the classical shallow water model (left) and for the shallow water model with porosity (right). Note that the coarse mesh in the model with porosity follows the contour of the urbanized zone (bold grey line in the figure on the right-hand side).

particular, the oscillations of the free surface along profiles 1 and 2 in the classical shallow water model are due to the presence of the blocks that obstruct the flow and cause local perturbations in the water level. Obviously, such details cannot be represented in the porosity model. Similarly, the local depression on the downstream side of the zone occupied by the blocks is due to local factors that cannot be represented by the model with porosity.

It is stressed that this should not be regarded as a failure of the porosity model, but as an inevitable consequence of the concept of porosity that is intended to reflect the macroscopic

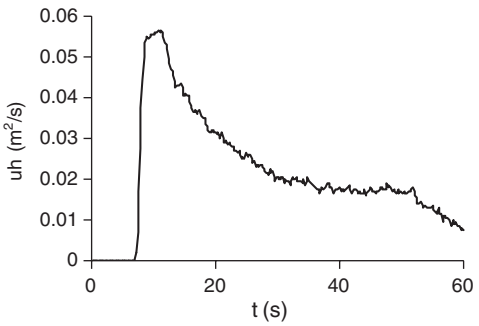

Figure 17. Unit discharge injected at the upstream boundary of the domain.

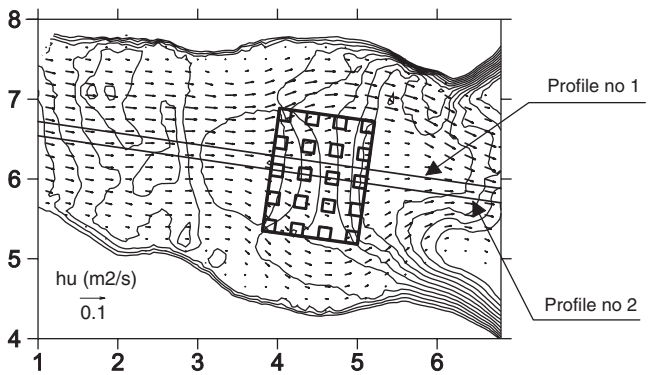

Figure 18. Plan view of the computed free surface elevations and unit discharges at $t = 20\,\mathrm{s}$ using the large scale model with porosity. Contour line spacing 0.01 m.

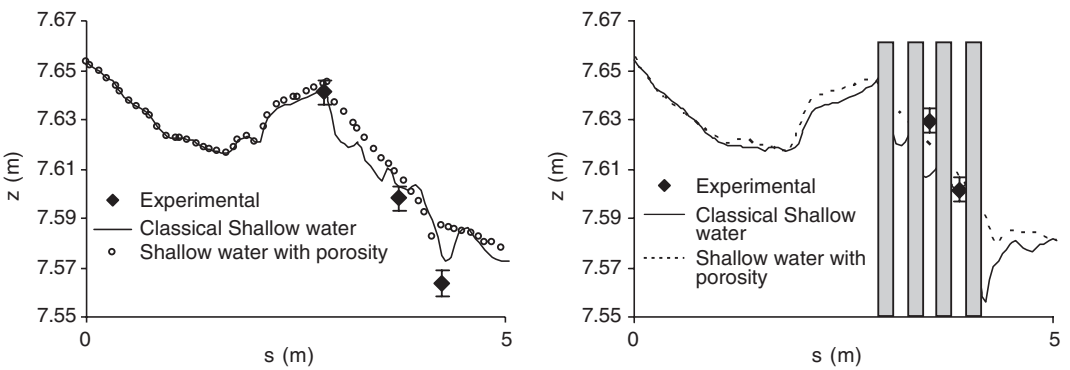

Figure 19. Longitudinal profiles of the free surface elevations computed at $t = 20\,\mathrm{s}$ using the refined model (solid line) and the coarse model with porosity (dots) along profiles 1 (left) and 2 (right). The error bars represent the measuring precision of the pressure gauges.

properties of the geometry. In contrast, the slope of the free surface, and therefore the head gradient, can be observed to be similar in both models, which indicates that the porosity concept is a viable alternative to the classical shallow water equations for the determination of the average flow characteristics in the urbanized area.

The comparison between the computed and measured water levels shows that the results of both the classical shallow water model and the porosity model match the measurements. The water levels seem to be overestimated by both models in the downstream part of the urban area along profile 1 and slightly underestimated by both models in the central part of the area in profile 2. It should be remembered however that the measurements consist of recorded bottom pressure and that multiple wave reflections and strongly curved flowpaths may cause the hydrostatic assumption not to be entirely valid in the close neighbourhood of the blocks. A point in favour of the shallow water model with porosity is that its results do not depart further from the experimental data than do the classical shallow water model results.

It should be noted that the 60 s simulation required 41 s CPU for the coarse model and 540 s CPU for the refined model on the same Pentium 4 processor. This example shows that large scale shallow water models with porosity may usefully contribute to the calculation of far-field flow conditions that can be used as boundary conditions for more refined flow models over urban areas.

5. CONCLUDING REMARKS

A modified Harten-Lax-van Leer (HLL) solver has been proposed for the solution of modified two-dimensional shallow water equations with porosity. When the porosity is uniform the modified equations are equivalent to the classical two-dimensional shallow water equations. The structure of the solution of the modified equations (number of waves and their propagation celerities, thus the stability criterion) is identical to that of the classical shallow water equations.

When the porosity is variable in space, an additional source term appears in the momentum equations and the classical formulation of the HLLC Riemann solver does not allow equilibrium and steady-state conditions to be satisfied. The modified solver allows steady-state solutions to be restored and is shown to perform well against analytical solutions in one and two dimensions of space with variable porosity. The comparison with the refined flow model of the Toce valley indicates that the concept of porosity is a viable option for the representation of the influence of urban areas in large-scale flow models. The authors admit not having expected such a good behaviour from the porosity model for the Toce application because of the small number of blocks (4×5) involved in the test. The concept of porosity, that is supposed to express a statistical property of the urban medium, was not expected to be meaningful at such a small scale.

The porosity can be easily determined *a priori* from maps or aerial photographs because it is a direct geometrical property of the medium. In the urban area the head loss is triggered to a small extent by bottom and wall friction and to a large extent by the multiple wave reflections against the urban structures and the local changes in the flow regime. A macroscopic head loss formulation based on the classical head loss formulae of hydraulics is proposed in the present paper.

In addition to the numerical treatment of the equations, future research and model validation should focus on methods for the determination of head loss coefficients from the geometrical characteristics of the urban zones. It also seems obvious that the fine tuning of such coefficients in real-world applications will require the comparison with historical records, as is already done for the determination of the Strickler coefficient in engineering studies with classical shallow water models.

APPENDIX A: DERIVATION OF THE MODIFIED SHALLOW WATER EQUATIONS AND THEIR DISCRETIZATION

The equations are derived by carrying out a mass and momentum balance over a rectangular volume $\mathrm{d}\Omega$ of horizontal and vertical dimensions δx and δy, respectively. The derivation of the continuity and the x-momentum equations are examined in Sections A.1 and A.2, respectively. The y-momentum equation being derived exactly in the same way as the x-momentum equation, devoting a separate subsection to its derivation is not necessary. Section A.3 deals with the discretization of the equations in conservation form on unstructured grids. In what follows, only the conservation part of the equations is dealt with.

A.1. The continuity equation

The continuity equation is derived first. The volume V of water contained in the control volume is given by

$$V = \int_{y_0}^{y_0+\delta y} \int_{x_0}^{x_0+\delta x} \phi(x, y) h \, \mathrm{d}x \, \mathrm{d}y \tag{A1}$$

where (x_0, y_0) are the coordinates of the lower left corner of the control volume. The volume fluxes $F_{V,\mathrm{W}}$ and $F_{V,\mathrm{E}}$ across the western and eastern sides, respectively, are given by

$$\begin{aligned} F_{M,\mathrm{W}} &= \int_{y_0}^{y_0+\delta y} (\phi h u_x)(x_0, y) \, \mathrm{d}y \\ F_{M,\mathrm{E}} &= \int_{y_0}^{y_0+\delta y} (\phi h u_x)(x_0 + \delta x, y) \, \mathrm{d}y \end{aligned} \tag{A2}$$

The discharges Q_{S} and Q_{N} across the southern and northern sides, respectively, are given by

$$\begin{aligned} F_{M,\mathrm{S}} &= \int_{x_0}^{x_0+\delta x} (\phi h u_y)(x, y_0) \, \mathrm{d}x \\ F_{M,\mathrm{N}} &= \int_{x_0}^{x_0+\delta x} (\phi h u_y)(x, y_0 + \delta y) \, \mathrm{d}x \end{aligned} \tag{A3}$$

The continuity equation can be written as

$$\frac{\partial V}{\partial t} = F_{M,\mathrm{W}} - F_{M,\mathrm{E}} + F_{M,\mathrm{S}} - F_{M,\mathrm{N}} \tag{A4}$$

Substituting Equations (A1)–(A3) into Equation (A4) gives

$$\frac{\partial}{\partial t}\int_{y_0}^{y_0+\delta y}\int_{x_0}^{x_0+\delta x}\phi(x,\,y)h\,\mathrm{d}x\,\mathrm{d}y-\int_{y_0}^{y_0+\delta y}(\phi hu_x)(x_0,\,y)\,\mathrm{d}y+\int_{y_0}^{y_0+\delta y}(\phi hu_x)(x_0+\delta x,\,y)\,\mathrm{d}y$$
$$-\int_{x_0}^{x_0+\delta x}(\phi hu_y)(x,\,y_0)\,\mathrm{d}x+\int_{x_0}^{x_0+\delta x}(\phi hu_y)(x,\,y_0+\delta y)\,\mathrm{d}x=0 \tag{A5}$$

that can be rewritten as

$$\int_{y_0}^{y_0+\delta y}\int_{x_0}^{x_0+\delta x}\frac{\partial}{\partial t}(\phi h)(x,\,y)\,\mathrm{d}x\,\mathrm{d}y+\int_{y_0}^{y_0+\delta y}[(\phi hu_x)(x_0+\delta x,\,y)-(\phi hu_x)(x_0,\,y)]\,\mathrm{d}y$$
$$+\int_{x_0}^{x_0+\delta x}[(\phi hu_y)(x,\,y_0+\delta y)-(\phi hu_y)(x,\,y_0)]\,\mathrm{d}x=0 \tag{A6}$$

When both δx and δy tend to 0 the following limits hold:

$$\begin{aligned}(\phi hu_x)(x_0+\delta x,\,y)-(\phi hu_x)(x_0,\,y)&\xrightarrow[\delta x\to 0]{}\delta x\frac{\partial}{\partial x}(\phi hu_x)\\(\phi hu_y)(x,\,y_0+\delta y)-(\phi hu_y)(x,\,y_0)&\xrightarrow[\delta x\to 0]{}\delta y\frac{\partial}{\partial y}(\phi hu_y)\end{aligned} \tag{A7}$$

and the integrals become equivalent to the product of the point values and the width of the integration interval. Therefore Equation (A6) becomes

$$\delta x\delta y\frac{\partial}{\partial t}(\phi h)+\delta y\delta x\frac{\partial}{\partial x}(\phi hu_x)+\delta x\delta y\frac{\partial}{\partial x}(\phi hu_y)=0 \tag{A8}$$

Dividing by $\delta x\delta y$ yields the continuity equation

$$\frac{\partial}{\partial t}(\phi h)+\frac{\partial}{\partial x}(\phi hu_x)+\frac{\partial}{\partial x}(\phi hu_y)=0 \tag{A9}$$

A.2. The momentum equation

The momentum equation is derived in the x-direction only. The y-momentum equation, that can be derived following exactly the same reasoning, will not be detailed here. The total x-momentum in the control volume is given by

$$M_x=\rho\int_{y_0}^{y_0+\delta y}\int_{x_0}^{x_0+\delta x}(\phi uh)(x,\,y)\,\mathrm{d}x\;\mathrm{d}y \tag{A10}$$

The x-momentum fluxes across the various edges of the control volume are given by

$$\begin{aligned} F_{M,\mathrm{W}} &= \rho \int_{y_0}^{y_0+\delta y} (\phi u_x^2 h)(x_0, y)\,\mathrm{d}y \\ F_{M,\mathrm{E}} &= \rho \int_{y_0}^{y_0+\delta y} (\phi u_x^2 h)(x_0+\delta x, y)\,\mathrm{d}y \\ F_{M,\mathrm{S}} &= \rho \int_{x_0}^{x_0+\delta x} (\phi u_x u_y h)(x, y_0)\,\mathrm{d}x \\ F_{M,\mathrm{N}} &= \rho \int_{x_0}^{x_0+\delta x} (\phi u_x u_y h)(x, y_0+\delta y)\,\mathrm{d}x \end{aligned} \tag{A11}$$

The external forces exerted in the x-direction on the water stored in the control volume are the following. The pressure force P_{W} is exerted from left to right on the western side of the control volume. It is given by

$$P_{\mathrm{W}} = \frac{\rho g}{2} \int_{y_0}^{y_0+\delta y} (\phi h^2)(x_0, y)\,\mathrm{d}y \tag{A12}$$

The pressure force P_{E} exerted from right to left on the eastern side of the control volume is given by

$$P_{\mathrm{E}} = -\frac{\rho g}{2} \int_{y_0}^{y_0+\delta y} (\phi h^2)(x_0+\delta x, y)\,\mathrm{d}y \tag{A13}$$

The reaction W_x exerted by the walls on the water body owing to the variation of the porosity in the x-direction is given by (see e.g. Reference [26] for a detailed proof)

$$W_x = \frac{\rho g}{2} \int_{y_0}^{y_0+\delta y} \int_{x_0}^{x_0+\delta x} \frac{\partial \phi}{\partial x} h^2\,\mathrm{d}x\,\mathrm{d}y \tag{A14}$$

The x-reaction B_x of the bottom to the weight of the water body per unit surface is the product of the local bottom pressure, the bottom slope in the x-direction and the porosity (because the reaction is exerted only at the points of the control volume occupied by the water).

$$B_x = -\rho g \int_{y_0}^{y_0+\delta y} \int_{x_0}^{x_0+\delta x} (\phi h)(x, y) \frac{\partial z_{\mathrm{b}}}{\partial x}\,\mathrm{d}x\,\mathrm{d}y \tag{A15}$$

The resistance R_x due to friction is accounted for by a classical Strickler law. The friction force is exerted only at the points occupied by the water

$$R_x = -\rho g h \int_{y_0}^{y_0+\delta y} \int_{x_0}^{x_0+\delta x} \left[\frac{(u_x^2 + u_y^2)^{1/2}}{K^2 h^{4/3}} \phi u_x \right] (x, y)\,\mathrm{d}x\,\mathrm{d}y \tag{A16}$$

The momentum balance can be written as

$$\frac{\partial M_x}{\partial t} = F_{M,\mathrm{W}} - F_{M,\mathrm{E}} + F_{M,\mathrm{S}} - F_{M,\mathrm{N}} + P_{\mathrm{W}} - P_{\mathrm{E}} + W_x + B_x + R_x \tag{A17}$$

It is first noted that in the limit of vanishing δx and δy, the differences between the fluxes and the forces at opposite edges of the control volume can be simplified as follows:

$$\begin{aligned} F_{M,\mathrm{W}} - F_{M,\mathrm{E}} &\underset{\delta x \to 0}{\approx} \rho \int_{y_0}^{y_0+\delta y} -\frac{\partial}{\partial x}(\phi u_x^2 h)\delta x \, \mathrm{d}y \\ F_{M,\mathrm{S}} - F_{M,\mathrm{N}} &\underset{\delta y \to 0}{\approx} \rho \int_{x_0}^{x_0+\delta x} -\frac{\partial}{\partial x}(\phi u_x u_y h)\delta y \, \mathrm{d}x \\ P_{\mathrm{W}} - P_{\mathrm{E}} &\underset{\delta x \to 0}{\approx} \frac{\rho g}{2} \int_{y_0}^{y_0+\delta y} -\frac{\partial}{\partial x}(\phi h^2)\delta x \, \mathrm{d}y \end{aligned} \tag{A18}$$

Substituting Equations (A14)–(A16) and Equation (A18) into Equation (A17) and dividing by ρ leads to

$$\begin{aligned} &\frac{\partial}{\partial t}\int_{y_0}^{y_0+\delta y}\int_{x_0}^{x_0+\delta x}(\phi u_x h)(x, y)\,\mathrm{d}x\,\mathrm{d}y + \int_{y_0}^{y_0+\delta y}\frac{\partial}{\partial x}(\phi u_x^2 h)\delta x\,\mathrm{d}y \\ &\quad + \int_{x_0}^{x_0+\delta x}\frac{\partial}{\partial y}(\phi u_x u_y h)\delta y\,\mathrm{d}x + \frac{g}{2}\int_{y_0}^{y_0+\delta y}\frac{\partial}{\partial x}(\phi h^2)\delta x\,\mathrm{d}y \\ &\quad = \frac{g}{2}\int_{y_0}^{y_0+\delta y}\int_{x_0}^{x_0+\delta x}\frac{\partial \phi}{\partial x}h^2\,\mathrm{d}x\,\mathrm{d}y - g\int_{y_0}^{y_0+\delta y}\int_{x_0}^{x_0+\delta x}(\phi h)(x, y)\frac{\partial z_{\mathrm{b}}}{\partial x}\,\mathrm{d}x\,\mathrm{d}y \\ &\quad\quad - gh\int_{y_0}^{y_0+\delta y}\int_{x_0}^{x_0+\delta x}\left[\frac{(u_x^2+u_y^2)^{1/2}}{K^2 h^{4/3}}\phi u_x\right](x, y)\,\mathrm{d}x\,\mathrm{d}y \end{aligned} \tag{A19}$$

Observing that the integral of a function tends to the product of the function point value and the size of the domain when the size of the domain tends to zero, (A19) is rewritten in the limit of δx, δy and δt tending to zero

$$\begin{aligned} &\delta x\delta y\frac{\partial}{\partial t}(\phi u_x h) + \delta x\delta y\frac{\partial}{\partial x}(\phi u_x^2 h) + \delta x\delta y\frac{\partial}{\partial y}(\phi u_x u_y h) + \delta x\delta y\frac{g}{2}\frac{\partial}{\partial x}(\phi h^2) \\ &\quad = \delta x\delta y\frac{g}{2}\frac{\partial \phi}{\partial x}h^2 - \delta x\delta y g\phi h\frac{\partial z_{\mathrm{b}}}{\partial x} - \delta x\delta y g h\frac{(u_x^2+u_y^2)^{1/2}}{K^2 h^{4/3}}\phi u_x \end{aligned} \tag{A20}$$

Dividing Equation (A20) by $\delta x\delta y$ yields

$$\begin{aligned} &\frac{\partial}{\partial t}(\phi u_x h) + \frac{\partial}{\partial x}\left(\phi u_x^2 h + \frac{g}{2}\phi h^2\right) + \frac{\partial}{\partial y}(\phi u_x u_y h) \\ &\quad = \frac{g}{2}\frac{\partial \phi}{\partial x}h^2 - g\phi h\frac{\partial z_{\mathrm{b}}}{\partial x} - g h\frac{(u_x^2+u_y^2)^{1/2}}{K^2 h^{4/3}}\phi u_x \end{aligned} \tag{A21}$$

A similar reasoning leads to the following equation for the y-momentum:

$$\frac{\partial}{\partial t}(\phi u_y h) + \frac{\partial}{\partial x}(\phi u_x u_y h) + \frac{\partial}{\partial y}\left(\phi v_y^2 h + \frac{g}{2}\phi h^2\right) = \frac{g}{2}\frac{\partial \phi}{\partial y}h^2 - g\phi h\frac{\partial z_b}{\partial y} - gh\frac{(u_x^2+u_y^2)^{1/2}}{K^2 h^{4/3}}\phi u_y \tag{A22}$$

The vector form of Equations (A9), (A21) and (A22) is Equation (1)

$$\frac{\partial}{\partial t}(\phi \mathbf{U}) + \frac{\partial}{\partial x}(\phi \mathbf{F}) + \frac{\partial}{\partial y}(\phi \mathbf{G}) = \mathbf{S}$$

with the definitions (2)–(4) for **U**, **F**, **G** and **S**.

A.3. Discretization and numerical solution

Equation (A1) is discretized using a finite volume formalism on unstructured grids. The continuity equation is discretized as

$$h_i^{n+1} = h_i^n - \frac{\Delta t}{\phi_i A_i}\sum_{j\in N(i)}\left[(\phi h u_x)_{i,j}^{n+1/2} n_{i,j}^{(x)} + (\phi h u_y)_{i,j}^{n+1/2} n_{i,j}^{(y)}\right] w_{i,j} \tag{A23}$$

where h_i^n is the average value of h over the cell i at the time level n, A_i is the area of the cell i, $(hu_x)_{i,j}^{n+1/2}$ and $(hu_y)_{i,j}^{n+1/2}$ are the average value of the x- and y-mass fluxes, respectively, at the interface (i,j) between the time levels n and $n+1$, $N(i)$ is the set of neighbour cells of the cell i, $n_{i,j}^{(x)}$ and $n_{i,j}^{(y)}$ are the x- and y-components of the normal unit vector (positive from i to j) to the interface $(i,j), w_{i,j}$ is the width of the interface (i,j), and Δt is the computational time step. The quantity $(\phi h u_x)_{i,j}^{n+1/2} n_{i,j}^{(x)} + (\phi h u_y)_{i,j}^{n+1/2} n_{i,j}^{(y)}$ represents the scalar product of the unit discharge and the normal unit vector, that is, the mass flux in the normal direction to the interface. Equation (A23) can be rewritten as

$$h_i^{n+1} = h_i^n - \frac{\Delta t}{\phi_i A_i}\sum_{j\in N(i)}(\phi h u)_{i,j}^{n+1/2} w_{i,j} \tag{A24}$$

where u is the velocity in the direction normal to the interface. This velocity is computed as in Equations (27)–(29) by solving a Riemann problem in the direction normal to the interface. The x- and y-momentum equation are discretized as follows. Solving the Riemann problem in the direction normal to the interface (i,j) yields the momentum fluxes F_ξ and F_ψ in the ξ- and ψ-directions, respectively. Such fluxes are defined as

$$\begin{aligned} F_\xi &= \left(\phi h u^2 + \phi\frac{g}{2}h^2\right)_{i,j}^{n+1/2} \\ F_\psi &= (\phi h u v)_{i,j}^{n+1/2} \end{aligned} \tag{A25}$$

where v is the velocity in the direction tangent to the interface. The fluxes are computed using Equations (30) and (43). The fluxes F_ξ and F_ψ at the interface (i,j) yield increases $(\Delta q_{\xi,i})_{i,j}$

and $(\Delta q_{\psi,i})_{i,j}$ in the ξ- and ψ-momentum in the cell i over a time step Δt

$$\begin{aligned}(\Delta q_{\xi,i})_{i,j} &= -F_\xi w_{i,j}\Delta t \\ (\Delta q_{\psi,i})_{i,j} &= -F_\psi w_{i,j}\Delta t\end{aligned} \tag{A26}$$

The increases $(\Delta q_{\xi,i})_{i,j}$ and $(\Delta q_{\psi,i})_{i,j}$ correspond to momentum increases $(\Delta q_{x,i})_{i,j}$ and $(\Delta q_{y,i})_{i,j}$ in the x- and y-directions, respectively

$$\begin{aligned}(\Delta q_{x,i})_{i,j} &= (\Delta q_{\xi,i})_{i,j} n_{i,j}^{(x)} - (\Delta q_{\psi,i})_{i,j} n_{i,j}^{(y)} \\ (\Delta q_{y,i})_{i,j} &= (\Delta q_{\xi,i})_{i,j} n_{i,j}^{(y)} + (\Delta q_{\psi,i})_{i,j} n_{i,j}^{(x)}\end{aligned} \tag{A27}$$

Substituting Equation (A26) into Equation (A27) leads to

$$\begin{aligned}(\Delta q_{x,i})_{i,j} &= -[F_\xi n_{i,j}^{(x)} - F_\psi n_{i,j}^{(y)}] w_{i,j}\Delta t \\ (\Delta q_{y,i})_{i,j} &= -[F_\psi n_{i,j}^{(x)} + F_\xi n_{i,j}^{(y)}] w_{i,j}\Delta t\end{aligned} \tag{A28}$$

The total increase in the x- and y-momentum in the cell i is obtained by summing up the individual contributions of all the edges (i, j) of the cell i

$$\begin{aligned}\Delta q_{x,i} &= \sum_{j\in N(i)} (\Delta q_{x,i})_{i,j} = -\sum_{j\in N(i)} [F_\xi n_{i,j}^{(x)} - F_\psi n_{i,j}^{(y)}] w_{i,j}\Delta t \\ \Delta q_{y,i} &= \sum_{j\in N(i)} (\Delta q_{y,i})_{i,j} = -\sum_{j\in N(i)} [F_\psi n_{i,j}^{(x)} + F_\xi n_{i,j}^{(y)}] w_{i,j}\Delta t\end{aligned} \tag{A29}$$

By definition, $\Delta q_{x,i}$ and $\Delta q_{y,i}$ also satisfy the following equalities:

$$\begin{aligned}\Delta q_{x,i} &= [(\phi h u_x)_i^{n+1} - (\phi h u_x)_i^n] A_i \\ \Delta q_{y,i} &= [(\phi h u_y)_i^{n+1} - (\phi h u_y)_i^n] A_i\end{aligned} \tag{A30}$$

Substituting Equation (A30) into (A29) and rearranging yields

$$\begin{aligned}(\phi h u_x)_i^{n+1} &= (\phi h u_x)_i^n - \frac{\Delta t}{A_i} \sum_{j\in N(i)} \left[F_\xi n_{i,j}^{(x)} - F_\psi n_{i,j}^{(y)}\right] w_{i,j} \\ (\phi h u_y)_i^{n+1} &= (\phi h u_y)_i^n - \frac{\Delta t}{A_i} \sum_{j\in N(i)} \left[F_\psi n_{i,j}^{(x)} + F_\xi n_{i,j}^{(y)}\right] w_{i,j}\end{aligned} \tag{A31}$$

Dividing by ϕ_i leads to

$$\begin{aligned}(h u_x)_i^{n+1} &= (h u_x)_i^n - \frac{\Delta t}{\phi_i A_i} \sum_{j\in N(i)} \left[F_\xi n_{i,j}^{(x)} - F_\psi n_{i,j}^{(y)}\right] w_{i,j} \\ (h u_y)_i^{n+1} &= (h u_y)_i^n - \frac{\Delta t}{\phi_i A_i} \sum_{j\in N(i)} \left[F_\psi n_{i,j}^{(x)} + F_\xi n_{i,j}^{(y)}\right] w_{i,j}\end{aligned} \tag{A32}$$

Given Equation (A25), Equations (A24) and (A32) can be written in vector form as

$$\mathbf{U}_i^{n+1} = \mathbf{U}_i^n - \frac{\Delta t}{\phi_i A_i} \sum_{j\in N(i)} \mathbf{P}_{i,j} (\phi \mathbf{F})_{i,j}^{n+1/2} w_{i,j} \tag{A33}$$

where **U**, **F** and **P** are defined as

$$\mathbf{U}=\begin{bmatrix} h \\ hu_x \\ hu_y \end{bmatrix}, \quad \mathbf{F}=\begin{bmatrix} hu \\ hu^2+gh^2/2 \\ huv \end{bmatrix}, \quad \mathbf{P}_{i,j}=\begin{bmatrix} 1 & 0 & 0 \\ 0 & n_{i,j}^{(x)} & -n_{i,j}^{(y)} \\ 0 & n_{i,j}^{(y)} & n_{i,j}^{(x)} \end{bmatrix} \tag{A34}$$

APPENDIX B: INTRODUCTION OF MACROSCOPIC HEAD LOSS FORMULATIONS IN URBANIZED AREAS

The objective of the present Appendix is to propose a formulation for the friction source term introduced in Equation (4), recalled here

$$\begin{aligned} S_{f,x} &= -\phi gh\frac{(u_x^2+u_y^2)^{1/2}}{K^2h^{4/3}}u_x - \phi ghs_x(u_x^2+u_y^2)^{1/2}u_x \\ S_{f,y} &= -\phi gh\frac{(u_x^2+u_y^2)^{1/2}}{K^2h^{4/3}}u_y - \phi ghs_y(u_x^2+u_y^2)^{1/2}u_y \end{aligned} \tag{B1}$$

where K is Strickler's friction coefficient, h is the water depth, $S_{f,x}$ and $S_{f,y}$ are the slopes of the energy line in the x- and y-directions, respectively, s_x and s_y are head loss coefficients accounting for the singular head losses due to the urban singularities in the x- and y-directions, respectively, u_x and u_y are the x- and y-flow velocities and ϕ is the porosity. The first term on the right-hand side of Equations (B1) represents the classical head loss due to friction against the bottom and walls under the wide channel approximation (i.e. the assumption that the water depth is small compared to the channel width, therefore leading to the equivalence between the hydraulic radius and the water depth).

Note that it would have been possible to propose a formulation accounting for the head loss via a single, equivalent Strickler (or Manning, or Chezy) coefficient. Such a formulation however is not felt appropriate because in classical Strickler-, Manning- or Chezy-like formulations, friction is assumed to result from the turbulent shear stress within the boundary layer at the bottom and walls and therefore be proportional to the wetted perimeter (hence the presence of the hydraulic radius in Strickler's, Manning's and Chezy's formulae). In contrast, the head loss resulting from a singularity is assumed to be identical over the entire flow cross-section and should therefore simply be proportional to the square of the velocities involved, without any influence of the hydraulic radius. This is for instance the case of Borda-like formulae that express the head loss across a sudden change in the flow cross-sectional area. Attempting to account for such head losses via an equivalent Strickler coefficient would make the equivalent Strickler coefficient depend on the hydraulic radius (here, the water depth), which is not the desired behaviour for such a coefficient. This is why the formulation (B1) is proposed instead, where s_x and s_y can be computed from the local characteristics of the flow and urban geometry.

In the application to the Toce test case s_x and s_y were determined using Borda's formula. The impinging flood wave travelling roughly in a direction parallel to the streets, the flow pattern can be viewed as occurring in separate, parallel channels, the cross-sections of which

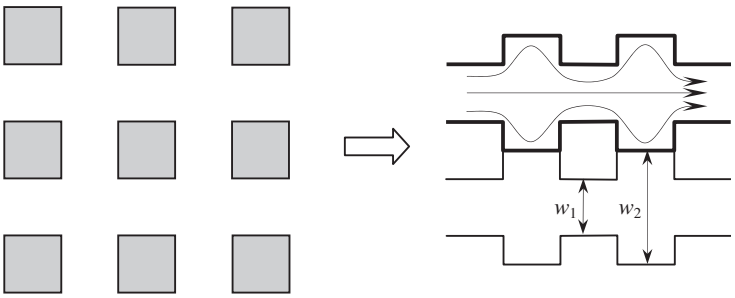

Figure B1. Representation of the urban flow pattern using parallel channels.

are subject to a periodic sudden widening and narrowing (Figure B1). The head loss ΔH_w is given by Borda's formula [27]

$$\Delta H_w = \frac{u_1^2 - u_2^2}{2g} \tag{B2}$$

where u_1 and u_2 are the velocities in the narrow and wide sections, respectively. Conservation of mass imposes

$$u_1 h_1 w_1 = u_2 h_2 w_2 \tag{B3}$$

where h_1 and h_2 are the water depths in the narrow and wide sections, respectively, and w_1 and w_2 are the widths of the narrow and wide sections, respectively. Since no distinction is possible between h_1 and h_2 in the porosity model, both are taken equal to the water depth h. Equation (B3) is then simplified into

$$u_1 w_1 = u_2 w_2 \tag{B4}$$

Substituting Equation (B4) into Equation (B2) and rearranging gives

$$\Delta H_w = \frac{w_2^2/w_1^2 - 1}{2g} u_2^2 \tag{B5}$$

In the Toce application u_2 was taken equal to the norm of the average flow velocity, which corresponds to the following modification for (B5):

$$\Delta H_w = \frac{w_2^2/w_1^2 - 1}{2g} (u_x^2 + u_y^2) \tag{B6}$$

The head loss ΔH_n across a sudden narrowing is given by [27]

$$\Delta H_w = \left[\left(\frac{1}{m} - 1 \right)^2 + \frac{1}{9} \right] \frac{u_1^2}{2g} \tag{B7}$$

where m is the so-called contraction coefficient, a recommended value for which is 0.62 [27]. Substituting Equation (B4) into Equation (B7) leads to

$$\Delta H_w = \left[\left(\frac{1}{m}-1\right)^2 + \frac{1}{9}\right]\frac{w_2^2}{w_1^2}\frac{u_2^2}{2g} \approx \left[\left(\frac{1}{m}-1\right)^2 + \frac{1}{9}\right]\frac{w_2^2}{w_1^2}\frac{1}{2g}(u_x^2+u_y^2) \tag{B8}$$

The sudden widening and narrowing being periodic in space, the slope of the energy line in the direction longitudinal to the flow is given by

$$\frac{\Delta H_w + \Delta H_n}{L} = \left\{\left[\left(\frac{1}{m}-1\right)^2 + \frac{10}{9}\right]\frac{w_2^2}{w_1^2} - 1\right\}\frac{u_x^2+u_y^2}{2gL} \tag{B9}$$

where L is the spatial period of the widening and narrowing. The slope of the energy line in the x- and y-directions is obtained by projection onto the x- and y-axes according to the velocity components. The final formula for s_x and s_y is

$$s_x = s_y = \left\{\left[\left(\frac{1}{m}-1\right)^2 + \frac{10}{9}\right]\frac{w_2^2}{w_1^2} - 1\right\}\frac{1}{2gL} \tag{B10}$$

ACKNOWLEDGEMENTS

This work was partly supported by a visiting grant from the Université catholique de Louvain-la-Neuve (Belgium).

REFERENCES

1. EC Contract EVG1-CT-2001-00037 IMPACT investigation of extreme flood processes and uncertainty. Available at www.impact-project.net
2. Alcrudo F, Garcia P, Brufau P, Murillo J, Garcia D, Mulet J, Testa G, Zuccala D. *The Model City Flooding Experiment*. EC Contract EVG1-CT-2001-00037 IMPACT investigation of extreme flood processes and uncertainty. *Proceedings of the 2nd Project Workshop*, Mo i Rana, Norway, September 2002 (CD-ROM).
3. Turner-Gillespie DF, Smith JA, Bates PD. Attenuating reaches and the regional flood response of an urbanizing drainage basin. *Advances in Water Resources* 2003; **26**:673–684.
4. Dutta D, Herath S, Musiake K. A mathematical model for flood loss estimation. *Journal of Hydrology* 2003; **277**:24–49.
5. Vieux BE, Bedient PB. Assessing urban hydrologic prediction accuracy through event reconstruction. *Journal of Hydrology*, in press.
6. Campana NA, Tucci CEM. Predicting floods from urban development scenarios: case study of the Diluviao Basin, Porto Alegre, Brazil. *Urban Water* 2001; **3**:113–124.
7. Defina A, D'Alpaos L, Mattichio B. A new set of equations for very shallow water and partially dry areas suitable to 2D numerical domains. *Proceedings Specialty Conference* '*Modelling of Flood Propagation over Initially Dry Areas*', Milano, Italy, 29 June–1 July, 2004.
8. Hervouet J-M, Samie R, Moreau B. Modelling urban areas in dam-break flood-wave numerical simulations. *Proceedings of the International Seminar and Workshop on Rescue Actions Based on Dambreak Flow Analysis*, Seinâjoki, Finland, 1–6 October, 2000.
9. Godunov SK. A finite difference method for the computation of discontinuous solutions of the equations of fluid dynamics. *Matematicheskii Sbornik* 1959; **47**:357–393.
10. Bermudez A, Vasquez-Cendron E. Upwind methods for hyperbolic conservation laws with source terms. *Computers and Fluids* 1994; **23**:1049–1071.
11. Gallouët T, Hérard J-M, Seguin N. Some approximate Godunov schemes to compute shallow-water equations with topography. *Computers and Fluids* 2003; **32**:479–513.
12. Bradford SF, Sanders BF. Finite-volume model for shallow-water flooding of arbitrary topography. *Journal of Hydraulic Engineering* 2002; **128**:289–298.

13. Zhou JG, Causon DM, Mingham CG, Ingram DM. The surface gradient method for the treatment of source term in the shallow-water equations. *Journal of Computational Physics* 2001; **168**:1–25.
14. Garcia-Navarro P, Vasquez-Cendron ME. On numerical treatment of the source terms in the shallow water equations. *Computers and Fluids* 2000; **29**:951–979.
15. LeVeque RJ. Balancing source terms and flux gradients in high-resolution Godunov methods, the quasi-steady wave-propagation algorithm. *Journal of Computational Physics* 1998; **146**:346–365.
16. Alcrudo F, Benkhaldoun F. Exact solutions to the Riemann problem of the shallow water equations with a bottom step. *Computers and Fluids* 2001; **30**:643–671.
17. Harten A, Lax PD, Van Leer B. On upstream differencing and Godunov-type schemes for hyperbolic conservation laws. *SIAM Review* 1987; **25**:35–61.
18. Toro EF, Spruce M, Speares W. Restoration of the contact surface in the HLL-Riemann solver. *Shock Waves* 1994; **4**:25–34.
19. Van Leer B. Toward the ultimate conservative difference scheme. IV. A new approach to numerical convection. *Journal of Computational Physics* **23**:276–299.
20. Toro EF. *Riemann Solvers and Numerical Methods for Fluid Dynamics*. Springer: Berlin, 1997.
21. Guinot V. *Godunov-Type Schemes*, *An Introduction for Engineers*. Elsevier: Amsterdam, 2003.
22. Davis SF. Simplified second-order Godunov-type methods. *SIAM Journal on Scientific and Statistical Computing* 1988; **9**:445–473.
23. Nujic M. Efficient implementation of non-oscillatory schemes for the computation of free-surface flows. *Journal of Hydraulic Research* 1995; **33**(1):101–111.
24. Guinot V. Linear advection modelling: the issue of strongly divergent flows. *Journal of Hydroinformatics* 2000; **2**:113–121.
25. Stoker JJR. *Water Waves*. Interscience: New York, 1957.
26. Cunge JA, Holly Jr FM, Verwey A. *Practical Aspects of Computational River Hydraulics*. Pitman Publishing: London, 1980.
27. Carlier M. *Hydraulique générale et Appliquée*. Eyrrolles: Paris, 1972.

